


# Dimerization and spin decoupling in a two-leg Heisenberg ladder with frustrated trimer rungs

 Andreas Weichselbaum<sup>1</sup>,\* Weiguo Yin, and Alexei M. Tsvelik

Condensed Matter Physics and Materials Science Division, Brookhaven National Laboratory, Upton, New York 11973, USA

 (Received 14 January 2021; accepted 10 February 2021; published 9 March 2021)

We study the antiferromagnetic spin-half Heisenberg ladder in the presence of an additional frustrating rung spin that is motivated and relevant also for the description of real two-dimensional materials such as the two-dimensional trimer magnet  $\text{Ba}_4\text{Ir}_3\text{O}_{10}$ . We study the zero-temperature phase diagram, where we combine numerical and analytical methods into an overall consistent description. All numerical simulations are also accompanied by studies of the dynamical spin structure factor obtained via the density matrix renormalization group. Overall, we find in the regime of strong rung coupling a gapped dimerized phase related to competing symmetry sectors in Hilbert space that ultimately results in frustration-driven spin-Peierls transition. In the weak rung-coupling regime, the system is uniform yet shows a gapped spinon continuum together with a sharp coherent low-energy branch that renders the system critical overall. In either case, the additional rung spin quickly gets sidelined and nearly decouples once its bare coupling to the ladder drops somewhat below the direct Heisenberg coupling of the legs.

 DOI: [10.1103/PhysRevB.103.125120](https://doi.org/10.1103/PhysRevB.103.125120)

## I. INTRODUCTION

In this paper, we study a model of a frustrated spin  $S = 1/2$  Heisenberg ladder antiferromagnet that is motivated by a quasi-one-dimensional (1D) reduction of the trimer magnet  $\text{Ba}_4\text{Ir}_3\text{O}_{10}$  [1–3]. That material is a member of the hexagonal perovskite family considered a potential host for quantum spin liquid behavior [4]. It consists of a layered structure with two-dimensional (2D) planes where trimer units interconnected into a quasihexagonal structure [cf. Fig. 1(b)]. The magnetism comes from trimer units that host three  $\text{Ir}^{4+}$  spin-half ions located within face-sharing octahedra. The dimensional reduction to 1D is partially justified by experimental indications, and it is consistent with an extremely low Néel ordering temperature  $T_N = 0.2$  K for the material where the bandwidth of the spin excitations by the Heisenberg couplings is several hundreds of Kelvin [3], thus spanning nearly four orders of magnitude in energy scales. As such, this material may be instrumental to the investigation of the long-standing speculation that 2D frustrated magnets might support quantum disordered states with neutral spin-half excitations known as spinons [5].

Our interest in this system is driven by its unusual spin arrangement, as schematically depicted in Fig. 1. This arrangement is conducive to several interesting effects. In its classical Ising limit, the system exhibits a frustration-driven ultranarrow phase crossover at finite temperature [6,7]. For the quantum case, as we will demonstrate in this work, the excitation spectrum contains a soft gapless mode separated from the other excitations by a gap in the limit of weak interchain coupling  $J_2, J_3 \ll J_1$ . The main contribution to the spectral weight of this mode comes from the central spins on the rungs. These spins nearly decouple from the system due to frustration, and they only experience an effective weak

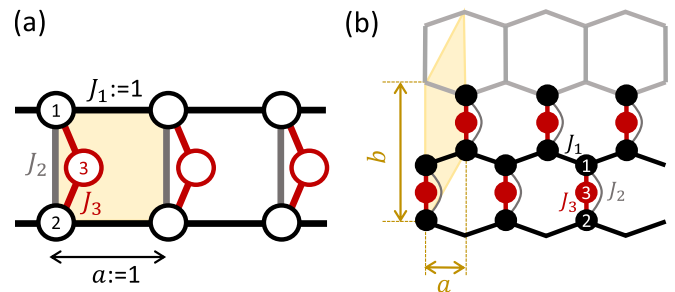


FIG. 1. The model system. (a) Two-leg Heisenberg ladder with trimer rungs and couplings  $J \equiv (J_1, J_2, J_3)$ . A rung consists of three spin  $S = 1/2$  sites, where  $m = 1, 2$  are the sites on the legs of the ladder. The presence of the additional *center* site on a rung (site  $m = 3$ ) coupled symmetrically to the leg sites via a finite coupling strength  $J_3$  induces frustration. (b) The same model may be seen to represent a hexagonal brick lattice with three-site rungs, using  $L_y = 2$  with the periodic boundary condition in the vertical direction. The lattice spacing of the three-site unit cell (yellow shaded area) is taken as  $a = 1$  (horizontally, in either case) or  $b$  [vertically, panel (b) only].

higher-order interaction among each other. As far as the spins located on the legs of the ladder are concerned, most of their spectral weight is located at higher energies, in agreement with experimental observations.

We point out that though the model looks like a version of a three-leg ladder that is expected to be equivalent to a spin-half chain and hence to be critical, this equivalence does not hold throughout the entire phase diagram. In the parameter range where the interchain interaction is frustrated, the “orbital” fluctuations are active and they may lead to dimerization [8–12], which is absent in spin-half chains.

The paper is organized as follows: In Sec. II we introduce the model. We then discuss first the strong rung-coupling regime in Sec. III, followed by the weak rung-coupling regime in Sec. IV. Each of these contains an analytical treatment

\*weichselbaum@bnl.gov

together with a complimentary density matrix renormalization group (DMRG [13,14]) analysis that also includes dynamical properties via the dynamical structure factor. Section V contains conclusions. Appendix A gives additional background on the downfolding to the effective low-energy Hamiltonian. Appendices B and C discuss an alternative, although not physically realized, possibility of an intermediate isotropic nematic phase with spontaneously broken rung mirror symmetry due to frustration.

## II. MODEL

We study the frustrated ladder model in Fig. 1, described by the Heisenberg Hamiltonian,

$$H = \sum_i \left[ \sum_{m=1,2} (J_1 \mathbf{S}_{im} \cdot \mathbf{S}_{i+1,m} + J_3 \mathbf{S}_{im} \cdot \mathbf{S}_{i3}) + J_2 \mathbf{S}_{i1} \cdot \mathbf{S}_{i2} \right] \equiv H^{\text{legs}}(J_1) + \sum_i H_i^{\text{rung}}(J_2, J_3), \quad (1)$$

with isotropic spin interactions, where rung  $i$  consists of three spin-half sites  $m=1, 2, 3$  described by the spin operators  $\mathbf{S}_{i,m}$ . The couplings  $(J_1, J_2)$  describe the regular ladder of two legs, whereas  $J_3$  couples the two legs to a third site  $m=3$  present for each rung and referred to as the *center site*, which thus frustrates the direct coupling in between the legs. We consider antiferromagnetic  $J_i > 0$  throughout. Moreover, we assume  $J_1 = 1$  as the unit of energy, unless specified otherwise, as well as  $\hbar = 1$ .

The Hamiltonian (1) has SU(2) spin symmetry, as well as up-down mirror symmetry as shown in Fig. 1(a), with the latter referred to as rung inversion or  $\mathbb{Z}_2$  parity symmetry. Within the analytical or mean-field approach, we assume periodic boundary conditions (BCs), whereas in the DMRG simulations we adopt open BCs, with the ladder terminated by rungs  $i=1$  and  $N$ . Overall, we are interested in the thermodynamic limit  $N \rightarrow \infty$ .

Taking  $J_3$  to zero reduces the system to the ordinary two-leg ladder, except for the presence of decoupled and thus free center spins. The latter would introduce macroscopic degeneracy. As will be shown, an approximate decoupling can also be achieved by frustration that, in practice, may give rise to spin freezing [15]. Also, one could introduce a Heisenberg interaction  $J'_1$  in between nearest-neighbor center spins in Fig. 1(a), thus resulting in a three-leg ladder. But such a coupling  $J'_1$  is considered negligible here, except for the discussion with Fig. 4. The motivation for this is that the center spins may not necessarily be nearest-neighbor (NN) spins after all, as compared to the leg spins. For example, one may assume that the center spins in Fig. 1(a) have a two-rung periodicity in that, e.g., they point into and out of the plane in an alternating fashion. Even more, when viewed as a minimal model for the decorated brick lattice in Fig. 1(b) assuming  $L_y = 2$ , the center sites are, indeed, very clearly far from being NN sites.

## III. THE LIMIT OF STRONG RUNG EXCHANGE

Let us start by focusing on a single rung consisting of three sites as marked in Fig. 1. This is relevant in the limit  $J_1 \rightarrow 0$ , i.e., dominating rung coupling, which reduces the system

to (nearly) decoupled trimers or triangles. Due to the SU(2) spin symmetry, the state space of a rung can be reduced from  $d = 2^3$  states to an effective dimension of  $d^* = 3$  multiplets, having two  $S = 1/2$  multiplets and one multiplet with  $S = 3/2$ . The latter is already symmetric under rung inversion. The two  $S = 1/2$  multiplets can be symmetrized, where the first is symmetric and the second asymmetric under rung inversion (by convention, the  $S = 1/2$  rung multiplet space will always be considered in this order). They will be denoted by  $|1/2\rangle^\pm$ . The antisymmetric multiplet  $|1/2\rangle^-$  forms a singlet across sites  $m = (1, 2)$ , with a free spin-half at site  $m = 3$ . The symmetric multiplet  $|1/2\rangle^+$  can be derived as a symmetric triplet on sites  $m = (1, 2)$  that when fused with site 3 also forms a total rung spin  $S = 1/2$ . The eigenstates of a single rung are thus divided into two groups: the low-energy space consisting of the two spin-full ‘‘orbitals’’  $|1/2\rangle^\pm$  at respective energies  $E_\pm^{(0)} = -\frac{\Delta_0}{2} \pm \frac{1}{2}(J_2 - J_3)$ , with  $\Delta_0 \equiv \frac{1}{2}(J_2 + 2J_3)$ , and the high-energy  $S = 3/2$  multiplet at energy  $+\frac{\Delta_0}{2}$ .

Frustration within each rung is therefore strongest when  $J_2 \approx J_3$ . In this case, the two orbitals  $|1/2\rangle^\pm$  become degenerate in energy. A finite detuning  $J_2 \neq J_3$  introduces an *orbital* splitting by an energy exactly equal to  $J_2 - J_3$ . This motivates the dimensionless parameter

$$\alpha \equiv \frac{J_2 - J_3}{J_1}. \quad (2)$$

The smaller the magnitude  $|\alpha|$ , the stronger the frustration.

The excitation energy from the low-energy states to the high-energy states is  $\Delta = \Delta_0 \pm \frac{\alpha J_1}{2}$ . For low enough temperatures  $T$  satisfying  $e^{-\Delta/T} \ll 1$  together with  $|\alpha| \ll 1$ , the thermal population of the high-energy  $S = 3/2$  multiplet vanishes. With the high-energy states irrelevant to the low-energy physics, we integrate it out by projecting the Hamiltonian of two nearest-neighbor rungs including their interaction along the legs into the low-energy space formed by the multiplet space  $|1/2\rangle^\pm$  using the many-body downfolding method [16–21] based on Hubbard operators [22]. To make the physics more apparent, we find it more convenient to represent these operators as products of Pauli matrices acting in the spin and effective orbital sector (see Appendix A for details), as is customary in theoretical studies of manganites with colossal magnetoresistance and many other materials with active orbital physics [21,23–28].

Since the strengths of the bare projection of the Hamiltonian for a nearest-neighbor pair of rungs and the second-order perturbative terms are proportional to  $J_1$  and  $J_1^2/\Delta_0$ , respectively [20], for strong rung-coupling  $J_1/\Delta_0 \ll 1$  it suffices to study the lowest order. This is described by the projected low-energy Hamiltonian,

$$\frac{1}{J_1} \mathcal{H}_\alpha^{\text{eff}} = \frac{8}{9} \sum_i (\mathcal{S}_i \cdot \mathcal{S}_{i+1}) \otimes \mathbb{T}_{i,i+1} + \alpha \sum_{i=1}^N \mathcal{T}_i^z, \quad (3a)$$

where given the two-leg ladder with center spins on the rungs we write  $\mathbb{T}_{i,i+1} = \mathbb{T}_{i,i+1}^{(2)}$ , we have

$$\mathbb{T}_{i,i+1}^{(2)} \equiv \frac{1}{4} + \frac{1}{2}(\mathcal{T}_i^z + \mathcal{T}_{i+1}^z) + \mathcal{T}_i^z \mathcal{T}_{i+1}^z + 3\mathcal{T}_i^x \mathcal{T}_{i+1}^x. \quad (3b)$$

Here  $\mathcal{S}_i^a \equiv \frac{1}{2}\sigma_i^a$  and  $\mathcal{T}_i^a \equiv \frac{1}{2}\tau_i^a$  are effective spin and orbital spin-half operators, respectively, with  $\sigma^a$  and  $\tau^a$  Pauli matrices with  $a \in \{x, y, z\}$ . These form the direct product

space  $\sigma \otimes \tau$  that acts on rung  $i$ . In fact, the new spin operators exactly correspond to the total spin operator on a rung,  $\mathcal{S}_i \equiv \mathbf{S}_i^{\text{tot}} \equiv \sum_{m=1}^3 \mathbf{S}_{im}$ , which, once projected onto the low-energy spin sector, indeed represent a plain proper spin operator acting on an  $S = 1/2$  spin degree of freedom.

The last term in Eq. (3a) is merely the aforementioned ‘‘orbital’’ splitting of  $\alpha J_1$ . It now functions as an effective magnetic field applied on the  $\tau$  pseudospins along the  $z$ -direction. It is offset by the linear  $\mathcal{T}_i^z$  term in Eq. (3b). The prefactor can be roughly estimated via a mean-field value for a decoupled Heisenberg chain [29,30], resulting in (cf. Appendix B)

$$\alpha_0 \equiv -\frac{8}{9} \langle \mathcal{S}_i \cdot \mathcal{S}_{i+1} \rangle \approx \frac{8}{9} \left( \ln 2 - \frac{1}{4} \right) = 0.394. \quad (4)$$

Therefore, only if  $\alpha \approx \alpha_0$  does the effective magnetic field become zero in the orbital sector. This offset also approximately agrees with the full many-body calculation, where the DMRG simulation in Fig. 2(c) shows that  $\alpha_0$  renormalizes to a slightly smaller value of 0.341.

The orbital magnetization  $\langle \mathcal{T}_i^z \rangle$  or  $\langle \mathcal{T}_i^x \rangle$  can be directly related to the intrarung spin-spin correlations,

$$C_{12}^{(i)} \equiv \langle \mathbf{S}_{i1} \cdot \mathbf{S}_{i2} \rangle = -\frac{1}{4} + \langle \mathcal{T}_i^z \rangle, \quad (5a)$$

$$C_{3+}^{(i)} \equiv \langle (\mathbf{S}_{i1} + \mathbf{S}_{i2}) \cdot \mathbf{S}_{i3} \rangle = -\frac{1}{2} - \langle \mathcal{T}_i^z \rangle, \quad (5b)$$

$$C_{3-}^{(i)} \equiv \langle (\mathbf{S}_{i1} - \mathbf{S}_{i2}) \cdot \mathbf{S}_{i3} \rangle = \sqrt{3} \langle \mathcal{T}_i^x \rangle, \quad (5c)$$

where  $\langle \dots \rangle$  denotes thermodynamic average. Equation (5a) shows that  $\langle \mathcal{T}_i^z \rangle$  measures whether the two-leg spins (1,2) are ferromagnetically or antiferromagnetically correlated. In fact,  $\langle \tau_i^z \rangle \equiv 2 \langle \mathcal{T}_i^z \rangle$  measures the rung parity  $\mathbb{Z}_2$ , where based on Eq. (5a),  $\tau_i^z$  acts like a swap operator for the two-leg sites. Conversely,  $\langle \mathcal{T}_i^x \rangle$  measures the  $\mathbb{Z}_2$  symmetry breaking between the leg spins if present. As seen from Eq. (5c), a nonzero value indicates a spontaneous breaking of the mirror symmetry between the upper and lower leg.

As an aside, we note that when the site-specific spin operators themselves are fully projected into the low-energy space, caveats apply, e.g., for sum rules. Since  $\mathcal{S}_i = \mathbf{S}_i^{\text{tot}}$  is fully constrained to the  $S = 1/2$  spin sector, one obtains  $\mathcal{S}_i^2 = \frac{3}{4}$ . However, if the site-specific spin operators  $\mathbf{S}_{im}$  themselves are fully projected to the low-energy  $S = 1/2$  space, then  $\sum_{m=1}^3 \mathbf{S}_{im}^2 = \frac{5}{4}$  (and not  $3 \times \frac{3}{4}$ , as this misses weight not of interest from intermediate excitations into the high-energy  $S = 3/2$  multiplet), such that the sum rule becomes  $(\mathbf{S}_1 \cdot \mathbf{S}_2 + \mathbf{S}_1 \cdot \mathbf{S}_3 + \mathbf{S}_2 \cdot \mathbf{S}_3)_i = \frac{1}{2} \left( \frac{3}{4} - \frac{5}{4} \right) = -\frac{1}{4}$ . In the absence of intermediate truncation in the spin operator products, as with Eqs. (5) above, this reads  $C_{12} + C_{3+} = -\frac{3}{4}$  instead.

The effective Hamiltonian (3) only includes nearest-neighbor terms derived from bare projection, which, at first glance, may be taken as an indication of a uniform ground state. In addition, one may also include next-nearest-neighbor (NNN) interactions via second-order perturbation. This translates the local rung frustration of the original ladder into frustration along the chain in the effective model. Such NNN interactions, while they leave the effective Hamiltonian translationally invariant, can be expected to generate dimerization as a relevant perturbation. This can give rise to spontaneous breaking of the translational symmetry along the chain [8,9]. Based on second-order perturbation, such a

symmetry breaking, however, should diminish in the limit of strong rung couplings  $J_2, J_3 \gg 1$ .

Nevertheless, as will be seen in the DMRG analysis below, the lowest-order projected Hamiltonian in Eq. (3) itself already gives rise to dimerization. Being at lowest order, the resulting dimerization also does not diminish but remains sizeable in the limit of strong rung couplings  $J_2, J_3 \gg 1$ . This suggests that spin and orbital degrees of freedom remain intrinsically entangled, and cannot be mean-field decoupled. The frustration of the spins on each rung in the original model is present via the (near) degeneracy of the two multiplets  $|1/2\rangle^\pm$ . One may argue that the decoupled spin chains described by the first term only in Eq. (3b) are subjected to relevant effective NNN order terms based on the remainder of the interactions in Eq. (3b). Therefore, overall, frustration is already intrinsic also to the effective projected Hamiltonian (3b).

Interestingly, dimerization as found in our DMRG simulations has been reported on an isotropic three-leg Heisenberg ladder in [11]. Translated to our model, this would turn on the coupling also for nearest-neighbor center sites ( $m = 3$ ). Taking it equally strong as for the initial two legs having  $J_1$ , then following the same downfolding procedure above, one obtains instead of Eq. (3b) the modified effective Hamiltonian in the orbital sector,

$$\mathbb{T}_{i,i+1}^{(3)} \equiv \frac{3}{8} + 3(\mathcal{T}_i^x \mathcal{T}_{i+1}^x + \mathcal{T}_i^z \mathcal{T}_{i+1}^z). \quad (6)$$

As compared to the two-leg case in Eq. (3b), the linear terms in  $\mathcal{T}^z$  disappeared [hence one also expects no offset here to the orbital magnetic field as estimated in Eq. (4)]. Also the  $\mathcal{T}^z \mathcal{T}^z$  term got strengthened, making it as strong as the  $\mathcal{T}^x \mathcal{T}^x$  term, which kept its prefactor unchanged. If one were to analyze the orbital sector effectively decoupled from the spin sector, this would result in a plain fermionic tight-binding chain after Jordan-Wigner transformation. On the contrary, however, the three-leg ladder mentioned above features dimerization instead [11]. This emphasizes the strongly correlated interplay between spin and orbital degrees of freedom. We will show below by continuously turning on the NN Heisenberg coupling on the center spins (cf. Fig. 4) that the spin gap observed with dimerization in the system never closes on the way, making an isotropic three-leg ladder with the same coupling  $J_1$  on all three legs. This suggests that the underlying physics is identical.

### A. Preliminary discussion

We proceed to discuss the physics of the effective strong-coupling Hamiltonian. The symmetries that can be spontaneously broken in the ground state are the  $\mathbb{Z}_2$  symmetry between the chains and the translational, or to be more precise, the inversion symmetry along the chains. Qualitative considerations suggest a possibility of the following  $T = 0$  phases. First, there are two diagonal, ‘‘orbital’’-ordered phases with  $\langle \mathcal{T}^z \rangle > 0$  and  $\langle \mathcal{T}^z \rangle < 0$ , respectively, which can coexist with translational symmetry breaking. There is the possibility of a nematic phase with spontaneously broken  $\mathbb{Z}_2$  symmetry, having  $\langle \mathcal{T}^x \rangle \neq 0$ . It is nematic, since with Eq. (5c) the local order parameter would consist of  $\mathbb{Z}_2$  symmetry-breaking variations in the energy density described by scalar products of spins

with the SU(2) spin symmetry itself preserved. The nematic order may coexist with translational symmetry breaking.

The diagonal phases appear at strong effective field  $|\alpha| \gg 1$  [cf. Eq. (2)], while also  $J_2, J_3 \gg 1$  ( $= J_1$ ). Then quantum orbital fluctuations in the  $xy$  orbital plane are suppressed. For  $\alpha \gg 1$ , i.e., dominant  $J_2 \gg J_3$ , the effective field via the last term in Eq. (3a) aligns,  $\langle T_i^z \rangle \simeq -1/2$ . By Eq. (5a), this results in the strongest possible antiferromagnetic correlation for the leg spins (1,2), such that they form an approximate singlet ( $S=0$ ), while the center spin becomes nearly decoupled. Overall, this is precisely the antisymmetric rung multiplet  $|1/2\rangle^-$ . On the other hand, for  $\alpha \ll -1$ , i.e., dominating coupling to the center spin,  $J_3 \gg J_2$ , the effective field in Eq. (3a) aligns  $\langle T_i^z \rangle \simeq 1/2$ . Again by Eq. (5), this shows that here the leg spins align ferromagnetically such that they form an approximate triplet ( $S=1$ ) with an antiferromagnetically aligned center spin. This is merely the symmetric rung multiplet  $|1/2\rangle^+$ .

In the latter diagonal phase for  $\alpha \ll -1$ , the spin dynamics in  $\mathcal{H}^{\text{eff}}$  is described by a simple single-chain spin-half Heisenberg model in terms of the symmetric multiplet  $|1/2\rangle^+$  and coupling strength of order  $J_1$ . As will be shown below, also the first diagonal phase ( $\alpha \gg 1$ ) reduces to an effective spin-half Heisenberg model in terms of the antisymmetric multiplet  $|1/2\rangle^-$ . There, however, this translates into a Heisenberg chain of weakly coupled center spins, such that in this case the coupling strength, and with it the energy scale of the spin dynamics, becomes vanishingly small for  $\alpha \gg 1$ .

The above analysis indicates that there may exist a quantum critical point (QCP) in the regime of weak  $|\alpha| < 1$  (i.e., strong spin frustration) that separates the two phases with antiferromagnetic and ferromagnetic correlations, respectively. Alternatively, there is also the possibility of a nematic phase for small  $\alpha$  whose phase boundaries would require two QCPs where the nematic order vanishes. The latter is suggested by a semi-mean-field approach as discussed in Appendix B. However, based on the detailed DMRG analysis presented below, neither turns out to capture the low-energy regime. Instead, the system favors a spontaneously broken translational symmetry with dimerization along the ladder that smoothly connects the regime  $\alpha \ll -1$  to  $\alpha \gg 1$ , as will be demonstrated next.

## B. Dimerization

In this section, we present extensive DMRG ground-state simulations on the two-leg ladder model in Eq. (1), as well as in its projected version in Eq. (3). The results are overall consistent, e.g., in that the total weight in the reduced density matrix for  $J_3 = 4$  in the local  $S = 3/2$  rung multiplet remained below 0.01 throughout. Here we use uniform ladders with open boundary conditions for  $J = (1, J_2, 4)$ , where we scan  $J_2$  and subsequently combine the data from the system center for each DMRG run at fixed  $J_2$ . Our results, with a focus on dimerization, are summarized in Fig. 2. Snapshots of the NN spin interactions are shown in Fig. 3 for  $J_2 = 4, 4.3$ , and 5. The DMRG data for these snapshots was obtained for a system size of  $L = 128$  rungs, with very minor variations as compared to  $L = 64$ , as seen in Figs. 2(a)–2(c). For clarity, we only show the left end, center, and right end of the ladder, with the intermediate regions cropped as indicated with the

lower axis sets. This demonstrates that the dimerization is well-established and uniform along the entire system.

Figures 2(a) and 2(b) analyze the NN spin correlations along the ladder,  $C_{mm'}^{(i,i+1)} \equiv \langle \mathbf{S}_{im} \cdot \mathbf{S}_{i+1,m'} \rangle$ , whereas Fig. 2(c) shows the perpendicular ones, i.e., within rungs. These interactions are computed based on the actual sites ( $m=1, 2, 3$ ), but in Figs. 2(a) and 2(c) also in terms of the effective spin operator  $\mathcal{S}_i$  (black line). By plotting data separately for even from odd bonds in the system center of the ladders analyzed, dimerization is absent if these curves lie on top of each other [e.g., Fig. 2(c)]. Dimerization develops where the curves split as in Fig. 2(a), where Fig. 2(b) plots the actual difference. Therefore, for a given parameter setting, dimerization starts around  $J_2 \gtrsim J_3 = 4$  [cf. Figs. 2(a) and 2(b)]. It develops a pronounced maximum around  $J_2 \sim 4.3$  [Fig. 2(b)] and drops again thereafter up to  $J_2 \sim 4.6$ . The dimerization ‘‘bubble’’ that opens between even and odd bonds in Fig. 2(a) is absent for Fig. 2(c), which analyzes the three bonds *within* a rung. The latter data is uniform when going from one rung to the next. Therefore, dimerization, and correspondingly spontaneous symmetry breaking, only exist along the legs, but not within the rungs.

The dimerization observed in the spin-spin correlations for  $J_2 \in [4, 4.5] \gtrsim J_3$ , and therefore  $\alpha \in [0, 0.5] \gtrsim 0$ , goes hand in hand with the appearance of a small but well-established spin gap  $\Delta_S \lesssim 0.15$  as shown in Fig. 2(d). There by simultaneously targeting multiple lowest-energy states in various global SU(2) symmetry sectors, we find that both the singlet and triplet gap are maximal for  $J_2 \simeq 4.31$  and are already well-converged to the aforementioned value for  $L = 64$  (light colors) as compared to  $L = 128$  (strong colors). While the ground state evolves smoothly, the excited states feature a sharp kink, which suggests a crossing of state spaces. This is natural, bearing in mind that the many-body Hilbert space can be partitioned into states that are either symmetric or antisymmetric under rung inversion symmetry and where their presence in the low-energy regime is expected to be reversed for  $J_2$  significantly larger or smaller as compared to  $J_3$ .

The location of the maximal spin gap coincides well with the crossing of weights for the symmetric and antisymmetric rung multiplet, as reflected by the crossing of the lines in Fig. 2(c): that crossing occurs at the exact point where the symmetric and antisymmetric rung multiplets,  $|1/2\rangle^+$  and  $|1/2\rangle^-$ , gain equal weight, since with Eq. (5) for  $m \neq m'$ ,  $\langle \mathbf{S}_{im} \cdot \mathbf{S}_{i,m'} \rangle = -0.25$  when  $\langle T_i^z \rangle = 0$ . As indicated with Fig. 2(c), the crossing occurs at  $J_2 \simeq 4.341$ , i.e.,  $\alpha_0^{\text{DMRG}} \simeq 0.341$ , which therefore slightly reduces the mean-field estimate for  $\alpha_0$  in Eq. (4). For  $J_2 \lesssim 4.2$ , the gap diminishes and dissolves within strong finite-size effects. The system appears critical and non-symmetry-broken for  $J_2 \lesssim J_3 = 4$  (e.g., see the center region in the upper panel of Fig. 3), even though based on the DMRG data we cannot exclude that a small but finite gap persists even for  $1 \ll (J_2 < J_3)$ .

The situation for large  $J_2 \gtrsim 4.6$  differs as compared to the case of small  $J_2 < J_3 = 4$ . By looking at Fig. 2, one notices two points: (i) the finite-size spacing in Fig. 2(d) is much smaller for large  $J_2 \gtrsim 4.6$  as compared to  $J_2 < 4$ , and (ii) while the dimerization in Fig. 2(b) diminishes on the actual legs of the ladder ( $m = 1, 2$ ), the dimerization starts to grow again for the center spins for  $J_2 \gtrsim 4.6$  (see also the lower

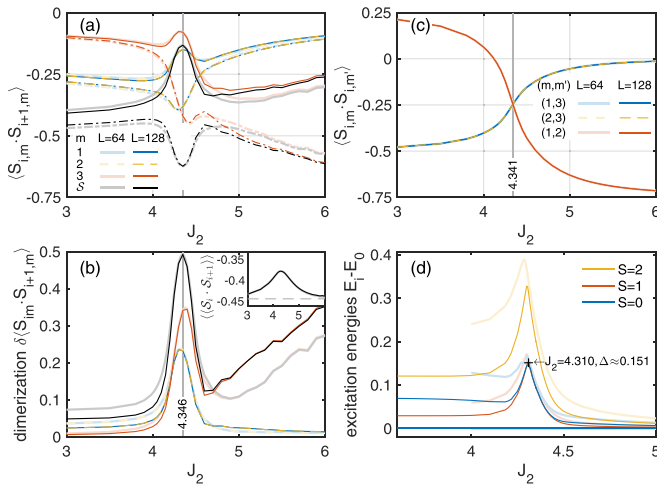


FIG. 2. Dimerization in the ladder model of Hamiltonian (1) in the strong rung-coupling limit, having  $J = (1, J_2, 4)$  vs  $J_2$  based on DMRG ground-state simulations for arbitrary but fixed  $J_2$  for  $L = 64$  (light thick lines) and  $L = 128$  (color matched thin dark lines). (a) NN interaction energies along the chain in the system center, showing even (odd) bonds around the system center separately as individual curves in solid (dashed-dotted), respectively. The data includes NN interaction in terms of the original spins with respect to sites  $m = 1, 2, 3$ , but also of  $S_i \equiv S_i^{\text{tot}}$ , as indicated with the legend. (b) Same as (a), also sharing the same legend, but plotting the difference between the even and odd bonds along the chain. The inset shows the average over even and odd bonds, denoted by  $\langle \langle \dots \rangle \rangle$ , vs  $J_2$  for the  $\langle S_i \cdot S_{i+1} \rangle$  data in (a). Here again the color-matched black line refers to  $L = 128$ , whereas the lighter gray line (mostly underneath the black line) refers to  $L = 64$ . The horizontal guide at the bottom of the inset indicates the analytically known expectation value for a plain spin-half Heisenberg chain,  $\frac{1}{4} - \ln(2)$  [cf. Eq. (4)]. (c) NN interaction energies within a rung in the system center. Same analysis as in (a), but here the data from even/odd rungs lies indistinguishably on top of each other. (d) Targeting lowest-energy states in global SU(2) spin sectors as indicated in the legend.

snapshot in Fig. 3 for  $J_2 = 5$ . Point (i) is fully consistent with the earlier discussion that for  $\alpha \ll -1$  ( $\alpha \gg 1$ ), which in the present case corresponds roughly to  $J_2 \lesssim J_3 = 4$  ( $J_2 \gtrsim 4.6$ ), respectively, the symmetric rung multiplet  $|1/2\rangle^+$  (or antisymmetric  $|1/2\rangle^-$ ) dominates the rung state space. This is clearly visible in the upper as compared to the lower snapshot in Fig. 3: the upper snapshot ties in all three spins on a rung based on antiferromagnetic correlations routed through the center spin. In contrast, the lower snapshot directly couples the leg spins, hence resulting in a dominant  $|1/2\rangle^-$ , which eventually results in these orbitals being gapped out, akin to a rung singlet phase in the plain Heisenberg ladder [31]. The residual center spins, however, only experience a very weak indirect coupling among each other via higher-order perturbative processes. Their effective spin-spin interaction diminishes to zero for  $J_2 \gg J_3$ , in qualitative agreement with the finite-size level spacing seen in Fig. 2(d).

Point (ii) is *a priori* unexpected. While all our DMRG data is very well-converged to start with (e.g., even for all the  $L = 128$  data, the ground-state energy is converged to well below  $10^{-6}$  relative accuracy throughout), there is room to believe that the eventual increase of the dimerization with the

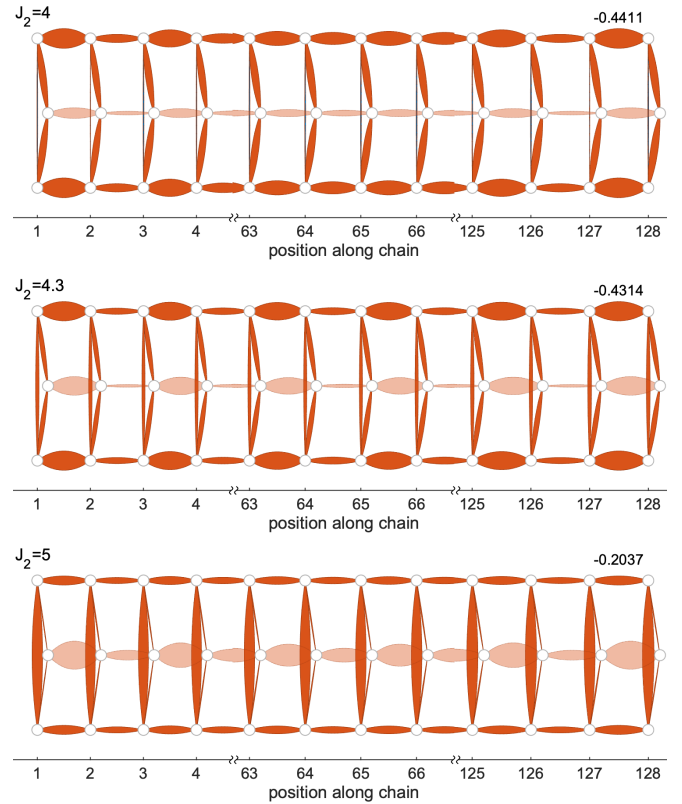


FIG. 3. Snapshots of NN bond strength  $C_{mm'}^{(i,i')} \equiv \langle S_{i,m} \cdot S_{i',m'} \rangle$  in the ladder model of Hamiltonian (1) for  $J = (1, J_2, 4)$  (same as in Fig. 2) with  $J_2$  as specified with the panel. The NN bond strength is drawn to scale proportional to the bond width (see the value for the bond at the upper right of each panel for reference). The NN interactions between center spins are shown as semitransparent (light colors) to indicate that no interactions are present in the Hamiltonian for these bonds. All bonds are of the same color, and hence of the same negative sign, thus being antiferromagnetically correlated. The data is for an  $L = 128$  ladder, showing left boundary, center, and right boundary, with the intermediate ranges cropped as indicated with each horizontal axis.

center spins in Fig. 2(b) is a numerical artifact. In fact, the DMRG simulations for  $J_2 \gtrsim 4.6$  were difficult to start with in that random initialization also randomizes the (very) weakly coupled center spins. This becomes very difficult to get rid of later toward a more uniform ladder, in that DMRG may be stuck within certain initial antiferromagnetic spin clusters with domain walls in between. Hence for  $J_2 \gtrsim 4.6$ , the DMRG was (also) initialized with a drastically down-sampled ground state obtained for smaller  $J_2 \sim 4.3$ . For the larger  $J_2$  values where a randomized starting state could still be afforded, the resulting data was overall consistent. Nevertheless, as seen from Fig. 2(b), the  $L = 64$  data shows a systematically smaller dimerization for  $J_2 \gtrsim 5$ , which may be attributed to the fact that the  $L = 64$  data is still overall systematically somewhat better converged than the  $L = 128$  data. So one may take this as a first indication that the dimerization seen with the center spins for large  $J_2$  shows a tendency to become smaller or even diminish altogether. In addition, the data for large  $J_2$  also shows some minor irregular, noisy behavior versus  $J_2$  for either system length  $L$ . This is mainly also attributed to

the quick decoupling of the center spins with increasing  $J_2$ . For similar reasons, the dimerization on the center spins may also be strongly influenced still by the presence of the open boundaries. The precise fate of the dimerization for large  $J_2$  therefore remains open, but there is room to believe that it diminishes for large  $J_2$  also for the center spins eventually. In this sense, in what follows we only refer to the intermediate range  $J_2 \sim J_3 + [0, 0.5]$  with  $J_3 \gg J_1 = 1$  as the (clearly) dimerized regime with the precise boundaries of this phase left for future studies.

The averaged correlations  $\langle\langle S_i \cdot S_{i+1} \rangle\rangle$  including both even and odd bonds are shown in the inset of Fig. 2(b). For  $J_2$  far detuned from  $J_3 = 4$ , this approaches the analytical value known for the plain spin-half Heisenberg chain indicated by the horizontal line. This clearly supports the overall picture that in the strong rung-coupling limit, the system effectively reduces to a plain spin-half Heisenberg chain, either in the symmetric or antisymmetric rung multiplet,  $|1/2\rangle^+$  or  $|1/2\rangle^-$ , for  $J_2 \lesssim J_3$  or  $J_2 \gtrsim J_3 + 0.6$ , respectively.

### C. Connection to the dimerized regime in a three-leg tube

The model of interest in this work is the two-leg ladder in Eq. (1), or its projected version in Eq. (3). Nevertheless, in the dimerized regime as in the center snapshot in Fig. 3, the center spins virtually correlate the same way as the leg spins, despite there being no direct coupling in between the center spins in the Hamiltonian at all [hence these bonds were depicted in semitransparent (light) colors]. Based on this, one may suspect that the dimerized phase persists even if a NN coupling is explicitly turned on also in between the center spins in the Hamiltonian. The resulting projected model results in the altered orbital Hamiltonian (6).

Figure 4 tracks the spin gap while turning on an explicit NN coupling  $J'_1$  in between center spins, starting around the maximal spin gap in the two-leg model at  $J = [1, 4.3, 4]$  at  $J'_1 = 0$  (cf. Fig. 2). Because the three-leg Hamiltonian in (6) has no linear offset to the orbital magnetic field as discussed with Eq. (4), at the same time as  $J'_1$  is turned on,  $J_2$  is tuned linearly toward  $J_3$ , i.e.,  $\alpha = 0$ , as indicated with Fig. 4. With this,  $J'_1 = 1 = J_1$  corresponds to a three-leg “tube” [10–12] with three equivalent legs, having  $J = [1, 4, 4]$ . As is evident from Fig. 4, the spin gap never closes; it even gets enhanced as  $J'_1$  is turned on. Hence the dimerization of the three-leg tube observed in Ref. [11] has the same physical character as the dimerized phase observed for the two-leg model here. Reference [11] analyzed the three-leg tube for any  $J_2 = J_3$  relative to  $J_1$ , which in the present case translates to  $\alpha^{\text{eff}} \equiv \alpha - \alpha_0 = 0$ . They argued that this model is always gapped and dimerized due to spin-frustration. Therefore, Fig. 4 shows that the dimerized regime seen in our model has the same physical origin, namely a frustration-induced spin-Peierls transition [32]. As we will demonstrate below, the spin-Peierls character of the dimerized phase is supported by the analytic calculations.

### D. Dynamical properties and crossover of spinon continua

The dynamical structure factor (DSF) examines the energetics of spin-spin correlations. Here we use it in the

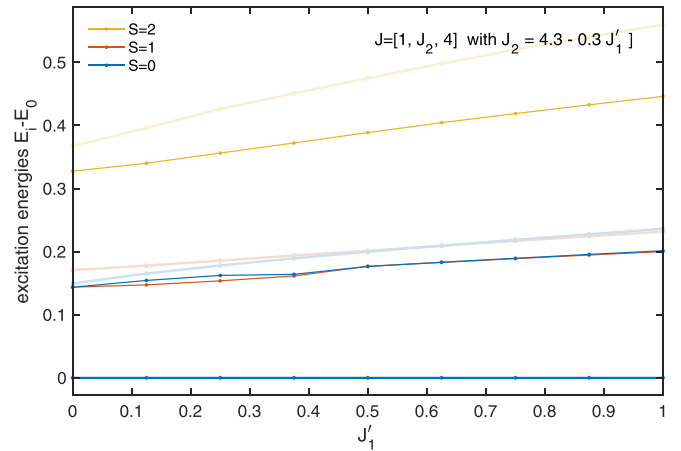


FIG. 4. Lowest-energy eigenstates of model (1) in the strong rung-coupling regime except that here, in addition, also a NN Heisenberg coupling  $J'_1 \in [0, 1]$  (horizontal axis) between the center spins was turned on. Therefore,  $J'_1 = 0$  well corresponds to the projected two-leg ladder in Eq. (3b).  $J_2$  was tuned with  $J'_1$  as indicated in the panel, such that  $J'_1 = 1$  corresponds to the uniform three-leg model with the projected low-energy orbital Hamiltonian as in Eq. (6). While the full, i.e., nonprojected rung state space was present in the simulations, the total weight of the  $S = 3/2$  multiplet was  $\lesssim 0.01$ , throughout. Light colors are for  $L = 64$ , whereas darker colors are for  $L = 128$ , similar to Fig. 2(d). States are color-coded according to their global  $SU(2)$  spin sectors as indicated in the legend.

form

$$S_{mm'}(k, \omega) = \sum_i e^{-ikx_i} \int dt e^{i\omega t} S_{mm'}(x_i, t), \quad (7)$$

where we only consider momentum  $k$  along the ladder, yet site-specific, and hence with real-space resolution along the “vertical” direction within a rung. Here  $x_i$  refers to the horizontal distance along the ladder using unit lattice spacing,  $x_i = i$ , with  $m$  and  $m'$  the local site indices within a rung, having  $S_{mm'}(x_i, t) \equiv \langle \mathbf{S}_{im}(t) \cdot \mathbf{S}_{0m'}(0) \rangle$  with site spins  $\mathbf{S}_{im}$  as in Eq. (1) with  $SU(2)$  spin symmetry intact. Here  $S_{0m'}$  refers to site  $m'$  on a reference rung at location  $i' = 0$ . In the present DMRG context, using open BCs, this always refers to a site on the center rung of the system. The DMRG prescription is then as follows: one performs real-time evolution [33,34], followed by double-Fourier transforms. To be specific, we subtract a static long-time background and perform zero padding in real space, followed by Fourier transform to momentum space. After careful linear prediction [35] of  $S(k, t)$  in time, the system is then also Fourier transformed to frequency space, followed by a final weak broadening to remove artificial speckles from pushing linear prediction. We emphasize that linear prediction in momentum space, and thus mixed coordinates  $(k, t)$ , is crucial, since for fixed  $k$  significantly fewer frequencies occur within  $S(k, t)$ . This is in stark contrast to  $S(x, t)$ , which has all frequencies from the entire DSF spectrum present, which then results in delayed, light-cone-like dynamics that is ill-suited for linear prediction.

The DSF obeys simple spectral sum rules. Frequency integration results in the static spin-spin correlation function,

whereas the fully integrated weight yields

$$\begin{aligned} S(S+1)I_{mm'} &\equiv \int \frac{dk}{2\pi} \int \frac{d\omega}{2\pi} S_{mm'}(k, \omega) \\ &= S_{mm'}(x_i = 0, t = 0) = \langle \mathbf{S}_{0m} \cdot \mathbf{S}_{0m'} \rangle. \end{aligned} \quad (8)$$

Here the prefactor was chosen such that in the present context of  $S = 1/2$  sites one obtains the normalized total weight,

$$I_{\text{tot}} \equiv \sum_{mm'} I_{m'm} = \frac{4}{3} \langle \mathbf{S}_0^{\text{tot}} \cdot \mathbf{S}_0^{\text{tot}} \rangle \equiv \frac{4}{3} \langle S_0^2 \rangle \gtrsim 1. \quad (9)$$

In the strong rung-coupling regime, where the local  $S = 3/2$  multiplet is effectively projected out, we have  $I_{\text{tot}} \simeq 1$ , which is assumed in the remainder of this section. The upper limit given by  $I_{\text{tot}} = 5$  holds for the hypothetical case in which the  $S = 3/2$  rung multiplet dominates. In the weak rung-coupling regime discussed later, we will encounter  $1 \leq I_{\text{tot}} \lesssim 2$ .

In the presence of dimerization, the structure factor as defined in Eq. (7) becomes complex [while  $S_{mm'}(x, \omega)$  is still real because the ground state can be taken real for our model, the Fourier transform in real space becomes complex due to the broken inversion symmetry]. In this case, we take the real part of the right-hand side of Eq. (7), which in the presence of dimerization is equivalent to symmetrization of the structure factor with respect to the location of site  $i' \in \{0, 1\}$ . The resulting DSF then is again symmetric for  $k \rightarrow -k$ , and also conforms to the standard momentum space definition and experimentally accessible DSF.

Within DMRG we start from real space, and hence full real-space resolution. We explicitly compute  $\langle \mathbf{S}_{im}(t) \cdot \mathbf{S}_{0m'}(0) \rangle = \langle 0 | \mathbf{S}_{im} \cdot [e^{-i(H-E_0)}(\mathbf{S}_{0m'}|0)] \rangle$ . With  $m, m', i' = 0$  fixed, the data is computed from real-time evolution and collected versus  $i$ . For simplicity, we sum the resulting data over the site index  $m$ . This corresponds to the spectral data at  $k_y = 0$  with respect to  $m$ , which is equivalent to using  $S_i$ . The resulting DSF,

$$S_{m'}(k, \omega) \equiv \sum_m S_{mm'}(k, \omega), \quad (10)$$

then refers to the spectral data resulting out of having acted with the initial spin operator on rung site  $m'$ . Since by the preserved mirror symmetry in the ground-state calculations it follows that  $S_1 = S_2$ , it suffices to compute  $S_1(k, \omega)$  and  $S_3(k, \omega)$  (e.g., as shown in Fig. 5). While much of  $S_{m'}(k, \omega)$  is dominated by  $m = m'$ , which results in a positive spectral density, it also contains an off-diagonal contribution  $m \neq m'$ . Therefore, if the local spin excitation induced at time  $t = 0$  preferentially propagates to a different rung site  $m \neq m'$ , then due to the underlying antiferromagnetic NN correlation, the spectral density of the DSF can turn negative for a particular range in momentum and frequency space. By properly combining  $S_1(k, \omega)$  and  $S_3(k, \omega)$ , however, the weighted average  $2S_1(k, \omega) + S_3(k, \omega)$  again must result in a non-negative spectral density throughout, as this represents the DSF now at  $k_y = 0$  for both  $m$  and  $m'$ , which is equivalent to computing the DSF based on  $\langle S_i(t) \cdot S_0(0) \rangle$ . Similarly, the respective total integrated spectral density is given by  $I_{\text{tot}} \equiv 2I_1 + I_3 \simeq 1$  [cf.

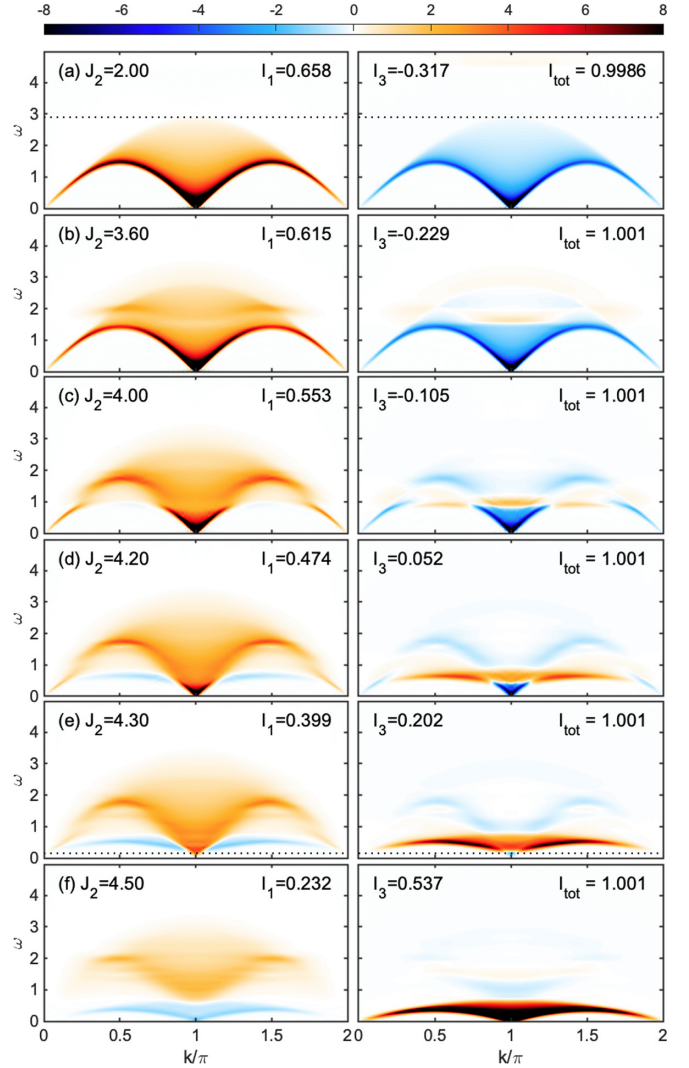


FIG. 5. Dynamical structure factor for the two-leg ladder (3) in the strong rung-coupling regime as in Fig. 2, having  $J = [1, J_2, 4]$  for various  $J_2$ , is indicated with the left panels top to bottom. The panel labels (a)–(f) each refer to a row that shares the same  $J_2$ . The left panels show  $S_1(k, \omega)$ , whereas the right panels show  $S_3(k, \omega)$  with the initial spin operator acting on site  $m' = 1$  or 3, respectively (see the text). The corresponding total integrated spectral density is also specified ( $I_1$  and  $I_3$ ), as well as the resulting total  $I_{\text{tot}} = 2I_1 + I_3$ . The color bar at the top holds for all panels. The spectral data is smoothed with  $\delta\omega = 0.05$  to remove speckles from linear prediction, except for  $J_2 = 4.3$ , which only uses half that value and which also shows a guide for the approximate spin gap at  $\omega = 0.15$  (dotted line). Panel (a) shows a guide at  $\omega \simeq 2.9$  that approximates the upper bound of the dominant spinon band. The weak superimposed wrinkly features as in (f) are attributed to state space truncation within the DMRG, and hence a numerical artefact.

Eq. (9)], which is well obeyed in the actual numerical data in the strong rung-coupling regime (cf. Fig. 5).

All DSF spectra presented here for the limit of large rung couplings are computed with the projected Hamiltonians, which have the  $S = 3/2$  rung state space removed, as this speeds up calculations considerably. This is justified given that the total weight of the  $S = 3/2$  multiplet states is typically

below 1% in ground-state calculations. Hence we only expect minor effects as a result of this simplification here, as verified in exemplary DSF calculations with the full rung state space kept (data not shown). Since the  $S = 3/2$  multiplet lies at high energy from the very outset here, having  $\Delta_0 \gtrsim 5$ , this simply means that faint spinon continua at high energy are absent, thus only marginally affecting spectral sum rules, while at the same time the DSF in the low-energy regime is well captured. Overall, the DSF results here are consistent with the ground-state DMRG analysis above based on the unprojected Hamiltonians, but they greatly compliment these by adding a dynamical perspective.

Our results for the DSF in the strong-coupling regime for the two-leg ladder (3) are summarized in Fig. 5, where left (right) panels show the DSF  $S_{m'}(k, \omega)$  for  $m' = 1$  (3), respectively. As explained above, the DSF shown can turn negative, but the combined total DSF,  $2S_1(k, \omega) + S_3(k, \omega)$ , is necessarily positive throughout, as verified (not shown). As a demonstration of the latter, we show that the total spectral density is well-normalized, with a well-obeyed spectral sum rule  $I_{\text{tot}} \simeq 1$  to good numerical accuracy throughout.

The DSF for  $J_2 = 2$  [row Fig. 5(a)] shows the behavior of a nearly pristine spin-half Heisenberg chain. Only a very faint higher-lying band is visible around  $\omega \sim 5$  in  $S_3$  (right panel). The clearly visible, dominant part of the spinon continuum is constrained within an upper bound of  $\omega \lesssim 2.9$  (dotted horizontal line), which is already within 4% of the expected value of  $(8/9)\pi$  for the limit  $1 \ll J_2 \ll J_3$ .

The very faint higher-lying band around  $\omega \sim 5$  in Fig. 5(a) actually relates to the state space of the symmetric rung multiplet  $|1/2\rangle^-$ . Having the effective orbital magnetic field  $\alpha - \alpha_0$ , its ‘‘Zeeman’’ splitting for Fig. 5(a) is  $2|\alpha - \alpha_0| \approx 4.6$ , which indeed coincides with the onset of the higher-lying band. Conversely, the low-energy spinon continuum originates from the symmetric rung multiplets  $|1/2\rangle^+$ . Now increasing  $J_2$  (going to lower rows in Fig. 5), the faint  $|1/2\rangle^-$  continuum at high energies moves downward in energy, such that it starts overlapping and interfering with the low-energy  $|1/2\rangle^+$  spinon continuum.

Their different origin also qualitatively translates into different signs in the DSF  $S_3(k, \omega)$ , and hence to different colors in the right panels of Fig. 5. There the  $|1/2\rangle^-$  spinon continuum appears positive (reddish), yet the  $|1/2\rangle^+$  spinon continuum appears negative (blueish). Hence by following the color coding in the right panels in Fig. 5 top to bottom, one can observe with increasing  $J_2$  toward  $J_3$  and above that the original  $|1/2\rangle^-$  spinon continuum at high energies crosses over with the  $|1/2\rangle^+$  spinon continuum at low energies, which itself then starts lifting off to higher energies. For the case in which the orbital magnetic field is approximately zero, e.g., at  $J_2 = 4.3$  in Fig. 5(e), both spinon sectors show a small but finite gap due to dimerization, with the earlier estimate for the spin gap  $\Delta_S \simeq 0.15$  marked by the vertical dotted line, and thus consistent with the dynamical spectral data. This scenario of *crossing state spaces* is also supported by analyzing ground-state entanglement spectra versus  $J_2$  (not shown).

For the largest  $J_2 = 4.5$  (Fig. 5), a different effective spin-half Heisenberg continuum has developed at low energies (dark red feature at the bottom right panel). This newly formed spinon continuum, however, now belongs to the antisymmet-

ric rung multiplet, and hence to the nearly decoupled center spins. Its bandwidth does not saturate, but it will diminish to zero when  $J_2$  is taken to  $J_2 \gg J_3$ . Since the leg spins are gapped out, this low-energy spinon continuum lives predominantly on the center spins. Hence  $S_3$  is dominated by  $m = m' = 3$  [cf. Eq. (10)], which is thus expected to be positive (reddish in color in Fig. 5, indeed).

### E. Mean-field theory for dimerized phase

If translational invariance is not spontaneously broken, then a mean-field argument suggests that the low-lying excitations in the spin sector are as in the uniform Heisenberg model. It is quantum critical and hence is susceptible to perturbations. The most likely relevant operator is the staggered energy density. This emerges as a result of spontaneous breaking of the translational symmetry resulting in dimerization. In the mean-field scheme, the staggered energy density in the spin sector emerges simultaneously with the staggered component of energy density in the orbital sector. The spin sector will certainly lose energy by the dimerization. Therefore, one has to look for a balance to establish whether or not the dimerized phase gains the overall lower energy.

To develop a mean-field theory for the dimerized phase, it is convenient to use Jordan-Wigner transformation in the orbital ( $\tau$ ) sector. Then with  $J_1 = 1$ , Eq. (3) becomes

$$\begin{aligned} \mathcal{H}_\alpha^{\text{eff}} &= \sum_i \left( \frac{8}{9} (\mathcal{S}_i \cdot \mathcal{S}_{i+1}) \otimes \mathbb{T}_{i,i+1}^{(2)} + i\alpha \chi_i \rho_i \right), \\ \mathbb{T}_{i,i+1}^{(2)} &= \underbrace{\frac{1}{4} + \frac{i}{2} (\chi_i \rho_i + \chi_{i+1} \rho_{i+1}) + \frac{3i}{2} \chi_i \rho_{i+1} - \chi_i \rho_i \chi_{i+1} \rho_{i+1}}_{\equiv \mathbb{T}_{i,i+1}^{(2)}}, \end{aligned} \quad (11)$$

where  $\chi_i = \frac{1}{\sqrt{2}}(c_i + c_i^\dagger)$  and  $\rho_i = \frac{i}{\sqrt{2}}(c_i^\dagger - c_i)$  are Majorana and thus real fermions that are subject to the anticommutation relations  $\{\chi_i, \chi_j\} = \{\rho_i, \rho_j\} = \delta_{ij}$ . Due to the reality of the Majorana fermions, Hamiltonian (3) is Hermitian as it stands, yet it may be symmetrized via  $\mathcal{H}_\alpha^{\text{eff}} = \frac{1}{2}(\mathcal{H}_\alpha^{\text{eff}} + \mathcal{H}_\alpha^{\text{eff}\dagger})$ . To simplify matters, we will omit the four-fermion (last) term above that corresponds to the  $\mathcal{T}^z \mathcal{T}^z$  term in Eq. (3b), as we do not aim for precision here, leaving this to the numerical calculations. This results in the mean-field approximation of Eq. (11),

$$H^{\text{MF}} \equiv \sum_i \beta_i (\mathcal{S}_i \cdot \mathcal{S}_{i+1}) + i \underbrace{\sum_i \chi_i \left( -\frac{3\alpha_i}{2} \rho_{i+1} + h \rho_i \right)}_{\equiv H_\tau} \quad (12a)$$

having

$$\alpha_i \equiv -\frac{8}{9} \langle \mathcal{S}_i \cdot \mathcal{S}_{i+1} \rangle \equiv \alpha_0 [1 + \delta(-1)^i], \quad (12b)$$

$$\beta_i \equiv \frac{8}{9} \langle \mathbb{T}_{i,i+1}^{(2)} \rangle \equiv \beta_0 [1 + \gamma(-1)^i], \quad (12c)$$

$$h \equiv \alpha - \frac{1}{2}(\alpha_{i-1} + \alpha_i) = \alpha - \alpha_0, \quad (12d)$$

with  $\alpha_0 \approx 0.394$  [cf. Eq. (4)]. Here  $\delta$  and  $\gamma$  are additional parameters to describe the strength of dimerization in the spin and orbital sector, respectively.

Further progress can be made assuming that the resulting spectral gap is small in comparison with the bandwidth,



which, as we will see, is consistent with the numerical calculations. Under this assumption, we can bosonize the spin part of (11). The uniform part of the Heisenberg Hamiltonian becomes the Gaussian model, and the staggered part is  $(-1)^i (\mathcal{S}_i \cdot \mathcal{S}_{i+1}) = A \cos(\sqrt{2\pi}\Phi)$ , where one can conclude from Ref. [36] that coefficient  $A \sim 1$ . Then we obtain the following sine-Gordon Lagrangian:

$$L_s^{\text{MF}} = \int dx \left[ \frac{1}{2v} (\partial_t \Phi)^2 + \frac{v}{2} (\partial_x \Phi)^2 - \frac{m_0^2}{2\pi} \cos(\sqrt{2\pi}\Phi) \right], \quad (13)$$

where  $v = \beta_0 \pi$  and  $m_0^2 = 2\pi A \gamma$ . This sine-Gordon model has a hidden SU(2) symmetry. Its excitations are massive, and consist of one massive triplet (soliton, antisoliton, and the first breather) with mass  $m_t \approx 0.893 m_0^{4/3}$  as can be extracted from [37], and the second breather with mass  $\sqrt{3} m_t$ . Then we have

$$\delta \sim \langle \cos(\sqrt{2\pi}\Phi) \rangle \approx 0.163 \sqrt{m_t} = 0.154 (A\gamma)^{1/3}. \quad (14)$$

Next we diagonalize the  $\tau$ -part of the Hamiltonian where we also aim to obtain a relation between the dimerization parameters  $\delta$  and  $\gamma$ . In momentum space with a two-site unit cell, the Hamiltonian assumes the matrix form

$$H_\tau = \sum_{k>0} \Psi^\dagger(k) H_\tau(k) \Psi(k),$$

$$H_\tau(k) = \frac{3i\alpha_0}{4} \begin{pmatrix} 0 & \tilde{h} & 0 & (1+\delta) \\ -\tilde{h} & 0 & (1-\delta)e^{-ik} & 0 \\ 0 & -(1-\delta)e^{ik} & 0 & \tilde{h} \\ -(1+\delta) & 0 & -\tilde{h} & 0 \end{pmatrix}, \quad (15)$$

where  $h \equiv \frac{3\alpha_0}{2} \tilde{h}$  and  $\Psi^T = ((\chi, \rho)_{A,k}, (\chi, \rho)_{B,k})$ . Its eigenvalues  $\varepsilon(k) \equiv \frac{3\alpha_0}{4} \tilde{\varepsilon}(k)$  out of  $\det(H_\tau - \varepsilon) = 0$  are given by

$$\tilde{\varepsilon}^2 = 1 + \delta^2 + \tilde{h}^2 \pm 2\delta_k, \quad (16)$$

with  $\delta_k^2 \equiv \delta^2 + \tilde{h}^2 [1 - (1 - \delta^2) \sin^2(\frac{k}{2})]$ . The dimerization  $\delta$  shifts the critical field and renormalizes the velocity, as seen by expanding around small  $k$ ,

$$\tilde{\varepsilon}^2 \simeq (1 \pm \sqrt{\delta^2 + \tilde{h}^2})^2 \mp \frac{(1 - \delta^2)\tilde{h}^2}{4\sqrt{\delta^2 + \tilde{h}^2}} k^2. \quad (17)$$

Now by making use of the Hellmann-Feynman theorem, we also have from Eqs. (12) above,

$$\begin{aligned} \frac{\partial}{\partial \delta} \langle H_\tau \rangle &= \langle \frac{\partial H_\tau}{\partial \delta} \rangle = -\alpha_0 \sum_i (-1)^i \frac{3i}{2} \langle \chi_i \rho_{i+1} \rangle \\ &= -\alpha_0 \frac{N}{2} \left( \langle \tilde{\mathbb{T}}_{2,3}^{(2)} \rangle - \langle \tilde{\mathbb{T}}_{1,2}^{(2)} \rangle \right) = -\frac{9N}{8} \alpha_0 \beta_0 \gamma. \end{aligned} \quad (18)$$

$= \frac{9}{8} (\beta_2 - \beta_1)$

Here in the orbital sector,  $\delta$  is considered an external parameter that gives rise to a finite orbital dimerization  $\gamma$ . Therefore,

$$\begin{aligned} \gamma &= \frac{8}{9\alpha_0\beta_0} \left( -\frac{1}{N} \frac{\partial}{\partial \delta} \langle H_\tau \rangle \right) \\ &= \frac{1}{9\alpha_0\beta_0\pi} \frac{\partial}{\partial \delta} \int_{-\infty}^{\infty} d\varepsilon \int_0^\pi \frac{dk}{2\pi} \ln \det[H_\tau(k) - i\varepsilon] \\ &\equiv \frac{B(\tilde{h})}{6\beta_0} \delta, \end{aligned} \quad (19a)$$

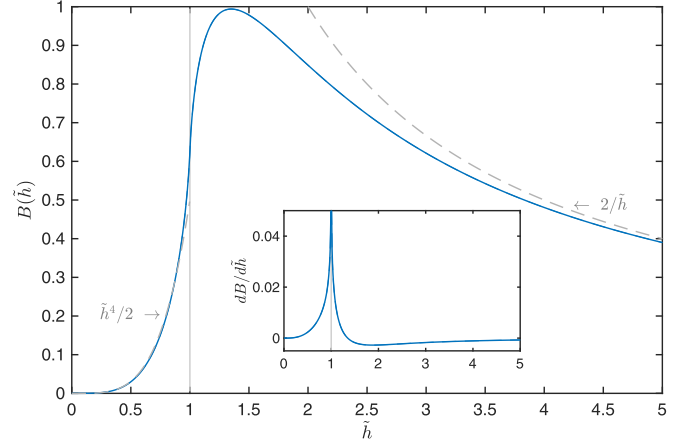


FIG. 6. The dimensionless function  $B(\tilde{h})$  from Eq. (19b). Dashed gray lines indicate asymptotic behavior. The inset shows a weak nonanalyticity at  $\tilde{h} = 1$  resulting in a vertical slope in main panel.

where

$$B(\tilde{h}) \equiv \int_0^\pi \frac{2dk}{\pi} \sum_{\sigma=\pm 1} \frac{1 + \sigma \frac{1 + \tilde{h}^2 \sin^2(k/2)}{\tilde{h} |\cos(k/2)|}}{(1 + \tilde{h}^2 + 2\sigma \tilde{h} |\cos \frac{k}{2}|)^{1/2}} \geq 0, \quad (19b)$$

where we expanded to linear order around  $\delta = 0$ . With Eq. (16),  $\langle H_\tau \rangle$  is an even function in  $\delta$ . Therefore,  $\gamma(\delta)$  is necessarily odd and hence, to lowest order, linear in  $\delta$ . Therefore, it also holds that  $B(\tilde{h}) \propto -\frac{\partial^2}{\partial \delta^2} \langle H_\tau \rangle$ . With  $h$  acting like an external magnetic field in the orbital sector, Eq. (19b) yields a linear relationship between the dimerization parameters  $\gamma$  and  $\delta$ . Matching this with the earlier relation in Eq. (14),  $\gamma \propto \delta^3$ , we get two solutions: (i) the nondimerized phase at  $\gamma = \delta = 0$ , as well as (ii) the nontrivial dimerized solution with  $(A\gamma)^{2/3} = A\gamma / (A\gamma)^{1/3} \simeq 0.154 A \gamma / \delta$ , i.e.,

$$(A\gamma)^{2/3} = 0.154 \frac{A}{6\beta_0} B\left(\frac{2h}{3\alpha_0}\right). \quad (20)$$

As seen in the numerical evaluation of the function  $B(\tilde{h})$  in Fig. 6, it vanishes quartically at  $\tilde{h} = 0$ , has a nonanalyticity with vertical slope at  $\tilde{h} = 1$ , followed by a maximum at  $\tilde{h}_c \sim 1.35$ , and then for large  $\tilde{h}$  decays like  $2/\tilde{h}$ . Hence there is an area of the phase diagram where the assumption  $\gamma \ll 1$  is valid, and so the current calculation is self-consistent.

Having  $B(\tilde{h}) \sim -\frac{1}{\delta} \frac{\partial}{\partial \delta} \langle H_\tau \rangle > 0$ , it follows that an orbital dimerization pattern that is aligned with the dimerization in the spin sector (in the sense that  $\gamma$  and  $\delta$  have the same sign) allows the orbital sector to *lower* its energy. Hence we conclude that the system favors dimerization, and in the strong-coupling limit a self-consistent dimerized solution always exists, at least for these somewhat simplified calculations with the  $\mathcal{T}^z \mathcal{T}^z$  term omitted. This conclusion is consistent with our DMRG data, which show a noticeable dimerization in the vicinity of  $|h| \ll 1$  (e.g., see Fig. 3).

#### IV. THE LIMIT OF WEAK RUNG EXCHANGE

In the limit of weak rung couplings, the full state space of the rungs needs to be included. Specifically, the  $S = 3/2$  symmetry sector can no longer be simply integrated out. In this section, we start with the theoretical description, followed

by DMRG simulations of the dynamical structure factor. The results are mutually consistent. In contrast to the strong rung-coupling regime above, we do not find any indication for dimerization here. Instead, we find a low-energy coherent branch. Consequently, there needs to be a quantum phase transition when decreasing  $J_2, J_3 \gg 1$  to small values  $J_2, J_3 < 1$ , the precise determination of which is left for future studies. By comparison, it may be noted that a fermionic model on the same lattice as in Fig. 1 in the weak rung-coupling regime also features flatbands that are predominantly associated with the weakly coupled center spins.

### A. Field theoretic approach

If the interchain exchange interactions are small,  $J_2, J_3 \ll J_1 = 1$ , we can use the continuum limit description. In this limit, the chains are described by the critical  $SU_1(2)$  Wess-Zumino-Novikov-Witten (WZNW) theories [38,39], and the interchain interaction and the interaction with the central spins are perturbations to this critical model. Both perturbations are relevant, but the interaction with the central spins is more relevant since it has scaling dimension  $1/2$  and the interchain coupling of the staggered magnetizations has dimension 1. We will consider the case when the interchain exchange is zero first.

Our derivation is a strict generalization of the one for a single chain coupled to dangling spins presented in [40]. We will reproduce it below with the appropriate modifications. The most convenient way is to combine the path integral representation for the middle spins with the field theory description for the legs. In this representation, the middle spins are replaced as  $\mathbf{S}_{0,j} = S_0 \mathbf{N}_j$ , where  $\mathbf{N}_j$  is a unit vector field with the Berry phase action. In the current context,  $S_0 = 1/2$ , but we prefer to keep it arbitrary for the time being. As far as the Heisenberg chains are concerned, at energies  $\ll 1$  we can use the field theory description, which is given by the  $SU_1(2)$  WZNW theory. The resulting action for energies  $\ll 1$  is given by

$$S = \sum_j S_0 A[\mathbf{N}_j] + W[g_1] + W[g_2] + i\gamma \sum_j (-1)^j \sum_{a=1,2} \int d\tau \mathbf{N}_j \text{Tr}[\bar{\sigma}(g_a^+ - g_a)], \quad (21)$$

where  $\mathbf{S}_0 = S_0 \mathbf{N}$ ,  $\mathbf{N}^2 = 1$ ,  $g_a(\tau, x)$  are the  $SU(2)$  matrix fields, and  $W[g]$  is the action of the  $SU_1(2)$  WZNW theory,  $A[\mathbf{N}]$  is the Berry phase, and  $\gamma \sim S_0 J_3$ . The Heisenberg spins are related to the WZNW fields,

$$\mathbf{S}_{j,a} = \frac{i}{2\pi} \text{Tr}(\bar{\sigma} g_a \partial_x g_a^+) + i(-1)^j C \text{Tr}[\bar{\sigma}(g_a - g_a^+)], \quad (22)$$

where  $C$  is a nonuniversal amplitude. The WZNW model is a critical theory with a linear excitation spectrum,  $\omega = v|k|$  with  $v = \pi J/2$ .

In the interaction term in (21) we kept only the most relevant term, which describes the interaction of the central spins with the staggered magnetization of the Heisenberg chains. This action is not yet what we need since the central spin variables remain lattice ones. To obtain the continuum limit, we have to integrate out the fast components of the central spins. We assume that at low energies these spins have a

short-range antiferromagnetic order, so we can write

$$\mathbf{N}_j = \mathbf{m}(x) + (-1)^j (1 - \mathbf{m}^2)^{1/2} \mathbf{n}(x), \quad x = a_0 j, \quad (23)$$

where  $\mathbf{n}^2 = 1$  and  $|m| \ll 1$ . The validity of this assumption is justified by the final result, which demonstrates that the correlation length of the middle spins is much larger than the lattice constant. Substituting this into (21) and following the well-known procedure [39,41], we obtain

$$S = \int d\tau dx \left\{ \frac{iS_0}{2} (\mathbf{n}[\partial_\tau \mathbf{n} \times \partial_x \mathbf{n}]) + iS_0 (\mathbf{m}[\mathbf{n} \times \partial_\tau \mathbf{n}]) + i\gamma (1 - \mathbf{m}^2)^{1/2} \text{Tr} \sum_a [(\bar{\sigma} \mathbf{n})(g_a - g_a^+)] \right\} + W[g_1] + W[g_2]. \quad (24)$$

Now notice that  $G = i(\bar{\sigma} \mathbf{n})$  is an  $SU(2)$  matrix. Hence,  $h_a = g_a G^+$  is also an  $SU(2)$  matrix, and we can use the identity [42]

$$W[hG] = W[h] + W[G] + \int \frac{d\tau dx}{2\pi} \text{Tr}(h^+ \partial h G \bar{\partial} G^+) \quad (25)$$

with  $\partial, \bar{\partial} = \frac{1}{2}(\partial_\tau \mp i v \partial_x)$ , so that the action (24) becomes

$$S = S_{\text{mass}} + S_m + S_n + \sum_a \int \frac{d\tau dx}{2\pi} \text{Tr}(h_a^+ \partial h_a G \bar{\partial} G^+), \quad (26a)$$

where

$$S_{\text{mass}} = W[h_1] + W[h_2] + \gamma \sum_a \int d\tau dx \text{Tr}(h_a + h_a^+), \quad (26b)$$

$$S_m = \int d\tau dx \left\{ \frac{D}{2} \mathbf{m}^2 + iS_0 (\mathbf{m}[\mathbf{n} \times \partial_\tau \mathbf{n}]) \right\}, \quad (26c)$$

$$S_n = 2W[i(\bar{\sigma} \mathbf{n})] + S_0 (\text{top-term}), \quad (26d)$$

$$S_{\text{top}} = \int d\tau dx \frac{i}{2} (\mathbf{n}[\partial_\tau \mathbf{n} \times \partial_x \mathbf{n}]), \quad (26e)$$

having

$$D = \gamma \sum_a \langle \text{Tr}(h_a + h_a^+) \rangle \sim \gamma^{4/3}. \quad (26f)$$

The latter estimate follows from the fact that the  $h$ -matrix operator in the  $SU_1(2)$  WZNW model has scaling dimension  $1/2$ . In a  $(1+1)$ -dimensional critical theory, a relevant perturbation with a scaling dimension  $d$  and coupling constant  $\lambda$  generates a spectral gap,  $\Lambda \sim \lambda^{1/(2-d)}$ . Consequently, the perturbation itself acquires a vacuum expectation value,  $\sim \Lambda^d \sim \lambda^{d/(2-d)}$ , giving rise to (26f).

Integrating over  $\mathbf{m}$  and taking into account that

$$W[i(\bar{\sigma} \mathbf{n})] = \frac{1}{2\pi} \int d\tau dx [v^{-1} (\partial_\tau \mathbf{n})^2 + v (\partial_x \mathbf{n})^2] + \frac{1}{2} S_{\text{top}}, \quad (27)$$

we obtain the effective Lagrangian density for the slow field  $\mathbf{n}$ :

$$\mathcal{L} = 1/2 \left( \frac{S_0^2}{D} + \frac{1}{\pi v} \right) (\partial_\tau \mathbf{n})^2 + \frac{v}{2\pi} (\partial_x \mathbf{n})^2 + \frac{iS_0}{2} (\mathbf{n}[\partial_\tau \mathbf{n} \times \partial_x \mathbf{n}]) \quad (28)$$

plus the action for the massive part for each  $a = 1, 2$ :

$$S_{\text{mass}} = W[h] + \gamma \int d\tau dx \text{Tr}(h + h^+) + \int d\tau dx \text{Tr}(\mathbf{J}_L[\mathbf{n} \times \bar{\partial}\mathbf{n}]). \quad (29)$$

This theory without the last term is, in fact, equivalent to the famous sine-Gordon model at the special value of the coupling constant  $\beta^2 = 2\pi$ . Indeed, the  $SU_1(2)$  WZNW model is equivalent to the Gaussian theory and  $\text{Tr}(h + h^+) \sim \cos(\sqrt{2\pi}\phi)$  such that

$$W[h] + \gamma \int d\tau dx \text{Tr}(h + h^+) = \int d\tau dx [1/2(\partial_\mu\phi)^2 - \tilde{\gamma} \cos(\sqrt{2\pi}\phi)]. \quad (30)$$

This theory is massive, and the spectrum consists of an  $SU(2)$  triplet with mass  $M \sim \gamma^{2/3}$  composed of sine-Gordon kink and antikink excitations and the first breather, and the second breather with mass  $\sqrt{3}M$ .

Note that the contribution to the topological term from (27) shifts the coefficient by 1, which is equivalent to 0. The mass gap  $\Lambda$  serves as the ultraviolet cutoff for the  $\sigma$  model (28). The corrections to the  $\sigma$  model generated by the last term in (29) carry a higher power of gradients of the  $\mathbf{n}$ -field, and therefore they can be discarded for momenta  $< \Lambda v^{-1}$ .

For the case relevant to this paper, the  $S_0 = 1/2$   $\sigma$  model (28) has a gapless spectrum in the same universality class as the  $S = 1/2$  Heisenberg chain [43]. This mode is slow since the corresponding velocity is

$$c^2 = \frac{v^2}{1 + \frac{2\tilde{\gamma}}{3\Lambda}}. \quad (31)$$

We emphasize that the above treatment is valid only in the region of energies much smaller than the excitation bandwidth. As is evident from the DMRG calculations, for most of the Brillouin zone the spectrum of the gapless mode is rather flat, which is consistent with the smallness of the velocity (31). The linear spectrum holds only in the vicinity of zero or  $\pi$  wave vectors. On the other hand, models describing rotated spins (29) have a spectrum with a gap  $\Delta_3 \cong J_3^{2/3}$  (all energies in units  $J_1 = 1$ ).

The spectral weight of the slow gapless mode is concentrated on the central spins, which is fully consistent with the results of the DMRG calculations displayed in Fig. 8. As for the spins located on the legs of the ladder are symmetric, and thus also in a phase with unbroken  $\mathbb{Z}_2$  symmetry. Substituting the expression for  $g = G^+h$  into (22), we get for the staggered magnetization

$$\mathbf{S}_{\text{stag}} \sim \mathbf{n}(\cos(\sqrt{2\pi}\phi)) + [\mathbf{n} \times \mathbf{K}], \quad (32)$$

$$\mathbf{K} = (\sin(\sqrt{2\pi}\phi), \cos(\sqrt{2\pi}\theta), \sin(\sqrt{2\pi}\theta)), \quad (33)$$

where  $\theta$  is the field dual to  $\phi$ . The correlation functions of the sine-Gordon model are well known; in particular, for this value of  $\beta$  the lowest part of the spectral weight consists of a coherent peak. As we can see from (32), in the spectral weight

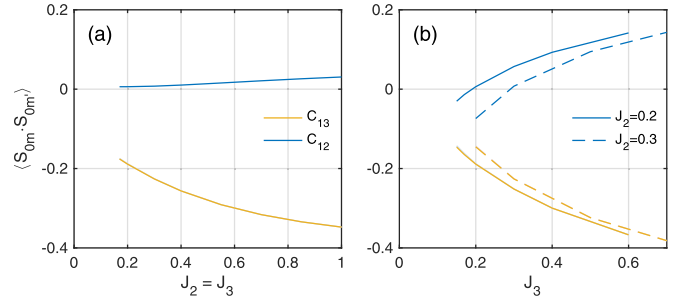


FIG. 7. Static spin expectation values  $C_{mm'} \equiv \langle \mathbf{S}_{im} \cdot \mathbf{S}_{im'} \rangle$  within the same rung  $i = 0$  in the system center of  $L = 64$  ladders with open BC for (a)  $(J_2 = J_3) \leq J_1 = 1$  and (b) vs  $J_3$  for fixed smaller  $J_2 \ll 1$  as indicated in the legend. The color coding in the legend in (a) holds for both panels.

of the leg spins this peak will be broadened by the emission of soft excitations of the  $\mathbf{n}$ -field. Such broadening cannot exceed the bandwidth of these excitations. Such a picture is consistent with Fig. 8.

The solution presented above is valid when the spectral gap of the “rotated” fields  $\Delta_3 \sim J_3^{2/3}$  is much larger than the spectral gap generated by the direct interchain exchange,  $\Delta_2 \sim J_2$ , i.e.,  $1 \gg J_3^{2/3} \gg J_2$  (all energies in units  $J_1 = 1$ ), and it holds only in the vicinity of the wave vectors 0 and  $\pi$  where excitations of the  $\mathbf{n}$ -field are gapless, in agreement with the DMRG. In fact, the opposite case,  $\Delta_3 \ll \Delta_2$ , would not differ qualitatively from this one. Indeed, the strong interchain coupling would generate a spectral gap in the spin-half ladder. Integrating out the gapped mode, we would get an effective exchange interaction between the central spins. These spins would then form a spin  $S = 1/2$  Heisenberg chain with gapless excitations. In both limits considered above, the spin-spin correlation functions of spins located on the legs of the ladder are symmetric. From a topological perspective, therefore, the weak-coupling limit is also trivial with no hidden order.

## B. Numerical analysis

In the weak rung-coupling regime, the legs of the ladder in the model system (1) tend to be weakly coupled from a static perspective. This is demonstrated via the static spin-spin correlators  $C_{mm'}^{(i)} \equiv \langle \mathbf{S}_{im} \cdot \mathbf{S}_{im'} \rangle$  between the sites of the same rung  $i = 0$  in the system center in Fig. 7. For  $J_2 = J_3$  [Fig. 7(a)], the direct leg-spin correlation,  $C_{12}$  (blue line), diminishes much faster than the correlation of the leg spins to the center spin (yellow line, same for both legs). For fixed small but finite  $J_2$ , tuning the coupling  $J_3$  [Fig. 7(b)] induces a sign change of the direct leg correlation  $C_{12}$ . Eventually, it saturates to a finite negative value for  $J_3 \rightarrow 0$  since  $J_2 > 0$ . At the same time, the correlation  $C_{13}$  to the center spin (yellow line, same for both legs) needs to vanish there. Hence the lines in Fig. 7(b) eventually cross for sufficiently small  $J_3$ .

The dynamical behavior in the weak rung-coupling regime is summarized in the DSF simulations presented in Fig. 8. These calculations are considerably more demanding numerically, since the full rung state space needs to be included. Clearly, for  $J_2, J_3 \lesssim 1$  the  $S = 3/2$  rung states are also expected to pick up considerable weight, hence they cannot be

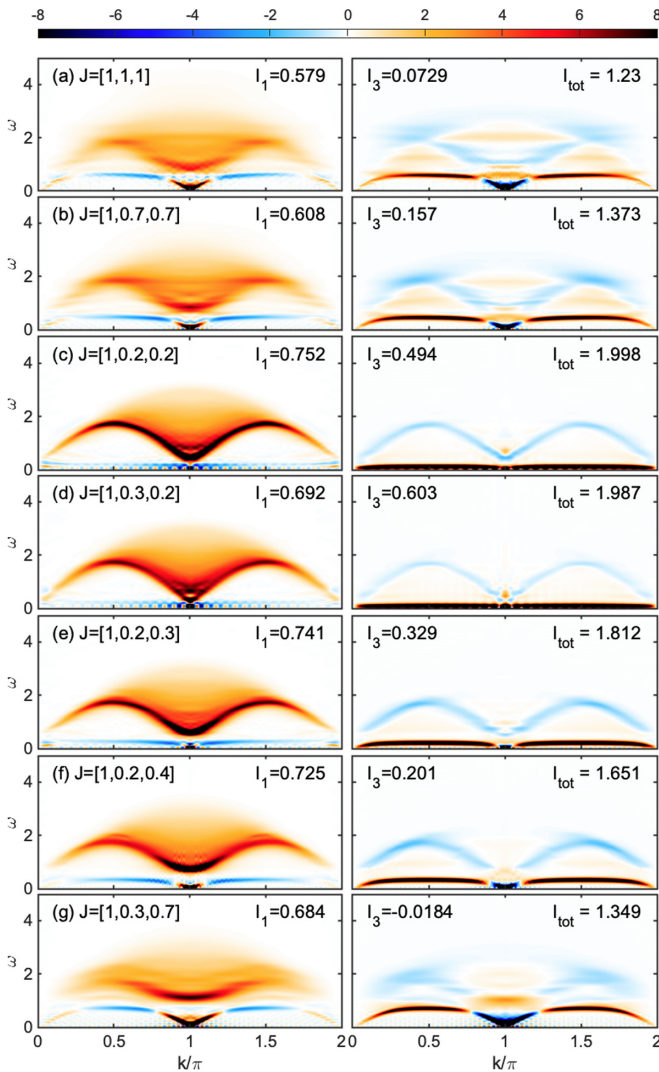


FIG. 8. Dynamical structure factor obtained via DMRG for the two-leg ladder (1) in the intermediate to weak rung-coupling regime for  $L = 64$  rungs [except for row (f), which has  $L = 128$ ]. The coupling strength is specified with the panels (panel label and  $J$  hold per row). Rows (a)–(c) have decreasing isotropic rung coupling  $J_2 = J_3$ . Rows (c)–(e) have  $J_2 < J_3 \ll 1$  with  $\alpha = 0$ ,  $\alpha < 0$ , and  $\alpha > 0$ , respectively. The remainder of the rows have  $\alpha > 0$  with increasing rung coupling. Exactly the same analysis as in Fig. 5 otherwise. In the present case, however,  $I_{\text{tot}} > 1$  indicates that there is also a significant admixture of the  $S = 3/2$  rung multiplet.

ignored. This is explicitly seen in Fig. 8 by having  $I_{\text{tot}} > 1$ , with the total weight in the  $S = 3/2$  given by  $(I_{\text{tot}} - 1)/4$  [cf. Eq. (9)]. Therefore, the simulations here are constrained to shorter ladders of length  $L = 64$ , except for row Fig. 8(f), which has  $L = 128$ . The affordable time range prior to Fourier transform is also more constrained, which translates into less overall spectral resolution. With the help of linear prediction, we can sharpen certain physical features in the DSF, but at the price of other “wrinkly” artificial features. Nevertheless, we preferred smaller subsequent broadening (same as in Fig. 5) over significant overbroadening of the data to completely smear out artifacts due to DMRG truncation. Also due to the shorter system size, discretization artifacts are also seen

versus momentum  $k$ . Bearing this in mind, we proceed to the physical interpretation of the results.

Within our energy resolution, all spectra are gapless. The low-energy regime of the DSF is dominated by a sharp coherent branch below the spinon continuum. Its energy quickly diminishes with decreasing  $J_2 \sim J_3 < 1$ , and it develops a close to flat dispersion over an extended momentum range (e.g., see the center rows in Fig. 5). It is much sharper in energy, and it does not show the energy spread typically seen with spinon continua. In this sense, the weak rung-coupling regime is qualitatively different from the crossings of the two spinon continua that were observed in the strong rung-coupling regime in Fig. 5. Similar to the strong rung-coupling regime, however, the low-energy branch here is also largely associated with the center spins, as implied by the sign (color) in the spectral data in the left versus right panels in Fig. 8. Specifically, we see a fainter negative (blue), yet a strong positive (dark red) spectral weight in the low-energy branch in the right panels, which relates to off-diagonal ( $m' \neq 3$ ) versus diagonal ( $m' = 3$ ) correlations, respectively.

The very flat branch close to zero energy as seen for  $J_2, J_3 \sim 0.2$  in the middle panels of Figs. 8(c)–8(e) nearly resembles static scatterers. Due to frustration, and the spectral data above, it can be argued that this is due to nearly decoupled center spins. Conversely then, from an experimental point of view, this coherent low-energy branch may be very difficult to distinguish from the static background that arises from actual impurities and imperfections in samples. In combination, it may also give rise to spin freezing [15] with reference to the magnetic moments on the center sites. Overall, the numerical results presented here are in qualitative agreement with the analytical discussion of the weak rung-coupling regime above.

## V. CONCLUSIONS

We have studied the model of a spin  $S = 1/2$  Heisenberg ladder with trimer rungs in the antiferromagnetic regime. The two legs of the ladder are coupled by a direct exchange, yet also indirectly, via an additional center spin for each rung, which introduces frustration. Many results are consistent with the general expectations. In particular, there is a significant part of the phase diagram where the spectrum of the spin excitations is gapless and critical belonging to the universality class of the spin  $S = 1/2$  Heisenberg antiferromagnet. The noteworthy feature is the presence of dimerization in the regime of strong rung coupling. For reference, the model studied can be considered as a version of a three-leg ladder with anisotropic rung coupling and where the coupling along the third leg is taken to zero. We numerically show that the dimerized phase in our model smoothly connects to the dimerized phase that has been previously reported on the isotropic three-leg ladder [11]. This provides support and further physical insight into our findings, namely that the dimerization is driven by a frustration-driven spin-Peierls transition [32].

In the regime of weak rung-coupling, we find a sharp coherent low-energy branch. It is largely associated with the center spins, which become nearly decoupled. This is consistent with the experimental observation in the trimer magnet  $\text{Ba}_4\text{Ir}_3\text{O}_{10}$  that we started out from, where the onset of AF ordering is deferred to extremely low temperatures as

compared to the estimated exchange energies [3]. Note that when returning to the 2D hexagonal model system in Fig. 1(b), the center spins in our quasi-1D reduction form an effective square lattice where Néel order eventually may be expected.

### ACKNOWLEDGMENT

Brookhaven National Laboratory was supported by U.S. Department of Energy (DOE) Office of Basic Energy Sciences (BES), Division of Materials Sciences and Engineering.

### APPENDIX A: MATRIX REPRESENTATION OF MANY-BODY DOWNFOLDING

Here we present a general method of many-body downfolding in matrix representation. We show the method by means of the specific example for the model Eq. (1). The basis set is given by the  $2^3 = 8$  states  $|S_1^z S_2^z S_3^z\rangle \equiv |S_1^z\rangle |S_2^z\rangle |S_3^z\rangle$  which form the direct product space of  $S_1 \otimes S_2 \otimes S_3$ , where  $S_m^z \in \{\uparrow, \downarrow\}$  denote spin up and down in a spin-half state. The orthonormal eigenvectors of  $H_i^{\text{rung}}$  are given by

$$\begin{aligned}
 |\Psi_1\rangle &\equiv |\tfrac{1}{2}, \tfrac{+1}{2}\rangle^+ = \frac{1}{\sqrt{6}} [ |(\uparrow\downarrow + \downarrow\uparrow)\uparrow\rangle - 2|\uparrow\uparrow\downarrow\rangle ], \\
 |\Psi_2\rangle &\equiv |\tfrac{1}{2}, \tfrac{-1}{2}\rangle^+ = \frac{1}{\sqrt{6}} [ -|(\uparrow\downarrow + \uparrow\uparrow)\downarrow\rangle + 2|\downarrow\downarrow\uparrow\rangle ], \\
 |\Psi_3\rangle &\equiv |\tfrac{1}{2}, \tfrac{+1}{2}\rangle^- = \frac{1}{\sqrt{2}} |(\uparrow\downarrow - \downarrow\uparrow)\uparrow\rangle, \\
 |\Psi_4\rangle &\equiv |\tfrac{1}{2}, \tfrac{-1}{2}\rangle^- = \frac{1}{\sqrt{2}} |(\uparrow\downarrow - \uparrow\uparrow)\downarrow\rangle, \\
 |\Psi_5\rangle &\equiv |\tfrac{3}{2}, \tfrac{+3}{2}\rangle = |\uparrow\uparrow\uparrow\rangle, \\
 |\Psi_6\rangle &\equiv |\tfrac{3}{2}, \tfrac{+1}{2}\rangle = \frac{1}{\sqrt{3}} |\uparrow\uparrow\downarrow + \uparrow\downarrow\uparrow + \downarrow\uparrow\uparrow\rangle, \\
 |\Psi_7\rangle &\equiv |\tfrac{3}{2}, \tfrac{-1}{2}\rangle = \frac{1}{\sqrt{3}} |\downarrow\downarrow\uparrow + \downarrow\uparrow\downarrow + \uparrow\downarrow\downarrow\rangle, \\
 |\Psi_8\rangle &\equiv |\tfrac{3}{2}, \tfrac{-3}{2}\rangle = |\downarrow\downarrow\downarrow\rangle,
 \end{aligned} \tag{A1}$$

where  $|1/2\rangle^\pm$  are the low-energy doubly degenerate  $S = 1/2$  multiplets with the eigenvalue of  $-\Delta_0/2 \pm \alpha J_1/2$ , with  $\Delta_0 \equiv \frac{1}{2}(J_2 + 2J_3)$ . They are symmetric (+) or antisymmetric (−) under rung exchange, i.e., exchange of sites  $m = 1, 2$ . They merge into a fourfold degeneracy at  $\alpha = 0$ . Otherwise, there exists an “orbital” splitting of  $\alpha J_1 \equiv J_2 - J_3$ . The remaining four states are the eigenvectors that form the high-energy  $S = 3/2$  multiplet with eigenvalue  $+\Delta_0/2$ , which are symmetric under rung exchange.

The excitation energy from the low-energy states to the high-energy states is  $\Delta(\alpha) = \Delta_0 \pm \alpha J_1/2$ . For the low-enough temperature  $T$  satisfying  $e^{-\Delta/T} \ll 1$  (i.e., vanishing thermal population of the four high-energy states) and  $\Delta/J \gg 1$  (i.e., little quantum fluctuations between these two groups), the high-energy states are irrelevant to the low-energy physics. Therefore, we project the Hamiltonian into the space formed by the four low-energy states using the many-body downfolding method [16–22] based on Hubbard operators [22]. For the Hamiltonian with spin-only operators, it is convenient to use the following matrix representation [20]. The eigenvectors in Eq. (A1) constitute the unitary transformation (also indicating

the order of states to the left),

$$U = \begin{matrix} \uparrow\uparrow\uparrow \\ \uparrow\uparrow\downarrow \\ \uparrow\downarrow\uparrow \\ \uparrow\downarrow\downarrow \\ \downarrow\uparrow\uparrow \\ \downarrow\uparrow\downarrow \\ \downarrow\downarrow\uparrow \\ \downarrow\downarrow\downarrow \end{matrix} \begin{pmatrix} 0 & 0 & 0 & 0 & 1 & 0 & 0 & 0 \\ -\frac{2}{\sqrt{6}} & 0 & 0 & 0 & 0 & \frac{1}{\sqrt{3}} & 0 & 0 \\ \frac{1}{\sqrt{6}} & 0 & \frac{1}{\sqrt{2}} & 0 & 0 & \frac{1}{\sqrt{3}} & 0 & 0 \\ 0 & \frac{-1}{\sqrt{6}} & 0 & \frac{1}{\sqrt{2}} & 0 & 0 & \frac{1}{\sqrt{3}} & 0 \\ \frac{1}{\sqrt{6}} & 0 & \frac{-1}{\sqrt{2}} & 0 & 0 & \frac{1}{\sqrt{3}} & 0 & 0 \\ 0 & \frac{-1}{\sqrt{6}} & 0 & \frac{-1}{\sqrt{2}} & 0 & 0 & \frac{1}{\sqrt{3}} & 0 \\ 0 & \frac{2}{\sqrt{6}} & 0 & 0 & 0 & 0 & \frac{1}{\sqrt{3}} & 0 \\ 0 & 0 & 0 & 0 & 0 & 0 & 0 & 1 \end{pmatrix}. \tag{A2}$$

The projection for any operator  $\hat{O}$  is done in the following procedure: Perform  $U^T \hat{O} U$  and retain the entries in the low-lying four-dimensional Hilbert space as the zeroth-order approximation and/or use the canonical transformation to get the higher-order terms [16–21]. The resulting  $4 \times 4$  matrices in the low-energy regime can be conveniently described by introducing two auxiliary spin  $S = 1/2$  operators

$$S^a = \frac{1}{2} \sigma^a \otimes 1^{(2)}, \tag{A3}$$

$$\mathcal{T}^a = 1^{(2)} \otimes \frac{1}{2} \tau^a, \tag{A4}$$

with  $\sigma^a$  and  $\tau^a$  the Pauli matrices, having  $a \in \{x, y, z\}$ , and  $1^{(2)}$  the  $2 \times 2$  identity matrix. Assuming that  $\sigma$  represents the fast index in  $\sigma \otimes \tau$  (also known as column major ordering), then given the state ordering in Eq. (A1), the  $S$  operators are spinlike because they operate within  $|\Psi_1\rangle$  and  $|\Psi_2\rangle$ , or within  $|\Psi_3\rangle$  and  $|\Psi_4\rangle$ , referred to as orbital 1 or 2, respectively. Conversely, the  $\mathcal{T}$  operators connect these two “orbitals” split by the energy  $\alpha J$ . Then, any projected operator  $\hat{O}$  can be written in the basis of the  $S$  and  $\mathcal{T}$  operators,

$$\begin{aligned}
 \hat{O}_{\text{projected}} &= U^T \hat{O} U \\
 &= f(I, S^x, S^y, S^z, \mathcal{T}^x, \mathcal{T}^y, \mathcal{T}^z),
 \end{aligned} \tag{A5}$$

where  $I$  is the  $4 \times 4$  identity matrix.

Since the strengths of the zero- and first-order terms are proportional to  $J$  and  $J^2/\Delta$ , respectively, it suffices for  $J/\Delta \ll 1$  to study the zeroth order, i.e., the plain projection into the low-energy regime [20]. The projected *interrung* interaction  $J$  terms in the zeroth-order approximation are given in Eq. (3). They can be obtained by using the projected spin operators in the zeroth-order approximation,

$$\begin{aligned}
 S_1^a &= \frac{2}{3} S^a (\tfrac{1}{2} I + \mathcal{T}^z + \sqrt{3} \mathcal{T}^x), \\
 S_2^a &= \frac{2}{3} S^a (\tfrac{1}{2} I + \mathcal{T}^z - \sqrt{3} \mathcal{T}^x), \\
 S_3^a &= \frac{2}{3} S^a (\tfrac{1}{2} I - 2\mathcal{T}^z),
 \end{aligned} \tag{A6}$$

with  $a \in \{x, y, z\}$ . The spin operators  $S^a$  have the simple interpretation that they exactly represent the total rung spin, i.e.,  $S \equiv \mathbf{S}_1 + \mathbf{S}_2 + \mathbf{S}_3 \equiv \mathbf{S}_{\text{rung}}^{\text{tot}}$ . With the low-energy space fully residing within the  $S = 1/2$  symmetry sector, this is indeed a well-defined spin-half operator. However, we stress that for the projection of the *intrarung* and general physical quantities, one should not use Eq. (A6). The correct way is to follow Eqs. (A2)–(A5), i.e., first do the exact transformation in the  $8 \times 8$  space and then do the reduction as the very last step. For example, in the correct way,  $S_{i,1}^2 = \frac{3}{4}$  is correctly reproduced

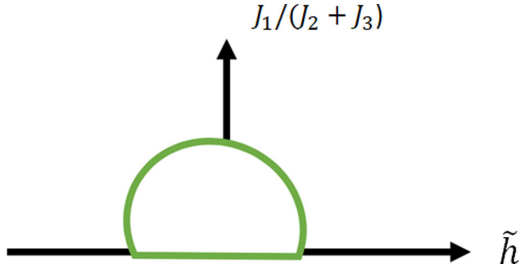


FIG. 9. Schematic phase diagram suggested by the SMF analysis vs  $J_1/(J_2+J_3)$  and effective orbital field  $\tilde{h} \sim \alpha \sim J_2 - J_3$ . The leg spins are ferromagnetically ( $\langle \mathcal{T}_i^z \rangle > 0$ ) and antiferromagnetically ( $\langle \mathcal{T}_i^z \rangle < 0$ ) aligned in the two phases  $\alpha \ll -1$  and  $\alpha \gg +1$ , respectively. They are separated by a phase with spontaneously broken  $\mathbb{Z}_2$  symmetry where  $\langle \mathcal{T}^x \rangle \neq 0$ .

in both the  $8 \times 8$  and  $4 \times 4$  matrix representations. In contrast,  $S_{i,1}^2 = \frac{5}{12}I + \frac{1}{3}\mathcal{T}^z + \frac{1}{\sqrt{3}}\mathcal{T}^x$  in the above-mentioned incorrect way. This is a consequence of the special algebra of Hubbard operators for on-site or intrarung actions [22].

#### APPENDIX B: MEAN-FIELD TREATMENT WITH TRANSLATIONAL INVARIANCE ENFORCED

Here we show that a semi-mean-field (SMF) treatment assuming a uniform, i.e., nondimerized state permits an entire intermediate phase with  $\langle \mathcal{T}^x \rangle \neq 0$  instead of a QCP at sufficiently small  $\alpha$ , as schematically depicted in Fig. 9. We stress, however, that eventually this is *not realized* in the many-body low-energy regime of the system, in that DMRG clearly finds a gapped dimerized ground state instead. Nevertheless, we believe this still represents an interesting point of view, hence we present it here in this Appendix. To start with the SMF treatment, we assume translational invariance, and we perform a mean-field decoupling of the spin from the orbital degrees of freedom [cf. Eqs. (3)],

$$\tilde{\mathcal{H}} = \tilde{\mathcal{H}}_{\text{spin}} + \tilde{\mathcal{H}}_{\text{orb}} - \tilde{\mathcal{E}}_0, \quad (\text{B1})$$

where

$$\tilde{\mathcal{H}}_{\text{spin}} \equiv \sum_i \tilde{J}_S \mathcal{S}_i \cdot \mathcal{S}_{i+1}, \quad (\text{B2a})$$

$$\tilde{\mathcal{H}}_{\text{orb}} \equiv \sum_i \left( -\tilde{J}_T (\mathcal{T}_i^z \mathcal{T}_{i+1}^z + 3\mathcal{T}_i^x \mathcal{T}_{i+1}^x) + \tilde{h} \mathcal{T}_i^z \right), \quad (\text{B2b})$$

$$\tilde{\mathcal{E}}_0 \equiv \frac{8J_1}{9} N \langle \mathcal{S}_i \cdot \mathcal{S}_{i+1} \rangle \langle \mathcal{T}_i^z + \mathcal{T}_i^z \mathcal{T}_{i+1}^z + 3\mathcal{T}_i^x \mathcal{T}_{i+1}^x \rangle, \quad (\text{B2c})$$

with the effective mean-field couplings

$$\tilde{J}_S \equiv \frac{8J_1}{9} \left( \frac{1}{4} + \mathcal{T}_i^z + \mathcal{T}_i^z \mathcal{T}_{i+1}^z + 3\mathcal{T}_i^x \mathcal{T}_{i+1}^x \right) \geq 0, \quad (\text{B3a})$$

$$\tilde{J}_T \equiv -\frac{8J_1}{9} \langle \mathcal{S}_i \cdot \mathcal{S}_{i+1} \rangle = \alpha_0 J_1 > 0, \quad (\text{B3b})$$

$$\tilde{h} \equiv J_1 \left( \alpha + \underbrace{\frac{8}{9} \langle \mathcal{S}_i \cdot \mathcal{S}_{i+1} \rangle}_{\equiv -\alpha_0} \right). \quad (\text{B3c})$$

Here Eq. (B2c) is just the mean-field reference energy, with the various local expectation values assumed independent of  $i = 1, \dots, N$ . The decoupled spin and orbital sectors, Eqs. (B2a) and (B2b), respectively, can be solved self-

consistently now given their respective quantum Hamiltonians (hence the terminology “semi-mean-field”). Having assumed translational invariance, the spin Hamiltonian (B2a) is always gapless. In contrast, for large  $|\tilde{h}|$ , the orbital Hamiltonian (B2b) is always gapped. Its ground state determines the active orbital in the spin Hamiltonian (B2a).

The resulting schematic SMF phase diagram, assuming a nondimerized phase, is depicted in Fig. 9. We shall briefly discuss its three phases. For the ground state of a spin-half Heisenberg chain, one has the exact result,  $\langle \mathcal{S}_i \cdot \mathcal{S}_{i+1} \rangle = \frac{1}{4} - \ln 2$  [29,30]. Therefore, assuming that the spin sector is close to its ground state, one obtains  $\alpha_0 \approx 0.394$  for  $T = 0$  [cf. Eq. (B3c)]. For the value  $\alpha = \alpha_0$ , then, i.e.,  $\tilde{h} = 0$ , the dominance of the symmetric or antisymmetric  $S = 1/2$  rung multiplet switches roles.

In the orbital sector, the Hamiltonian (B2b) has quantum critical points in the same universality class as the quantum Ising model with ferromagnetic interaction. The interaction strength for the  $\mathcal{T}_i^x \mathcal{T}_{i+1}^x$  term is three times as large as that for the  $\mathcal{T}_i^z \mathcal{T}_{i+1}^z$  term. In the continuum limit, the  $\mathcal{T}^z$  operator becomes a product of right- and left-moving Majorana fermions, and hence the term  $\mathcal{T}_i^z \mathcal{T}_{i+1}^z \sim \rho_i \chi_i \rho_{i+1} \chi_{i+1} \sim \rho \partial_x \rho \chi \partial_x \chi$  [cf. Eq. (11) in the main text] becomes highly irrelevant with a scaling dimension of  $d = 4$ . In the absence of the  $\mathcal{T}^z \mathcal{T}^z$  term, the criterion for the emergence of the symmetry-broken state with finite  $\langle \mathcal{T}^z \rangle$  can be estimated by [44]

$$\left| \frac{2\tilde{h}}{3\tilde{J}_T} \right| = \frac{2}{3} \left| \frac{\alpha - \alpha_0}{\alpha_0} \right| < 1, \quad (\text{B4})$$

given the critical field  $|\tilde{h}|_{\text{cr}} \simeq \frac{(3\tilde{J}_T)}{2}$  [cf. Eq. (B2b)]. This corresponds to  $\alpha \in \frac{\alpha_0}{2} [-1, 5] \approx [-0.197, 0.985]$ . The neglected  $\mathcal{T}^z \mathcal{T}^z$  term is expected to shift these boundaries, as motivated by a mean-field decoupling  $\mathcal{T}^z \langle \mathcal{T}^z \rangle$ .

Right at  $\tilde{h} = 0$ , the orbital Hamiltonian becomes a version of the  $XY$  model in zero magnetic field where exact results for the magnetization are available:  $\langle \mathcal{T}_i^x \rangle = \frac{\sqrt{2}}{3} \approx 0.471$  [45]. The state with a spontaneously broken  $\mathbb{Z}_2$  symmetry can be understood as the state where the center spins predominantly form singlets with a particular leg of the ladder that would translate into an asymmetry of correlation functions that include leg spins. When  $\alpha$  increases, the system undergoes a phase transition into the symmetric state with nonzero  $\langle \mathcal{T}_i^z \rangle$  where the above asymmetry disappears. For any finite temperature  $T$ , the symmetry is restored by thermal average, i.e., having  $\langle \mathcal{T}_i^x \rangle = 0$ , whereas  $\langle \mathcal{T}_i^z \rangle$  is proportional to the effective field when it is weak [44,45]. As a result, it does not contain a phase transition at finite temperature.

For large  $\tilde{h}$  the orbitals become strongly polarized, as discussed in the main text. With  $\langle \mathcal{T}_i^z \rangle \simeq \pm \frac{1}{2}$ , the effective spin coupling in Eq. (B3a) becomes  $\tilde{J}_S \simeq \frac{8J_1}{9} \left( \frac{1}{4} \pm \frac{1}{2} \right)$ , which thus motivates the positive sign indicated with Eq. (B3a). For example, for dominant  $J_2$ , i.e.,  $\alpha \gg +1$  with  $\langle \mathcal{T}_i^z \rangle \simeq -\frac{1}{2}$ , the center spins become nearly decoupled, which thus corresponds to a spin-half Heisenberg chain with vanishing effective coupling  $\tilde{J}_S \sim 0$  in the low-energy regime of the system. Conversely, for dominant  $J_3$ , i.e.,  $\alpha \ll -1$  with  $\langle \mathcal{T}_i^z \rangle \simeq +\frac{1}{2}$ , the low-energy behavior is described by a single effective Heisenberg chain with finite effective coupling  $\tilde{J}_S \simeq \frac{8J_1}{9}$ . Note that the same picture for large  $\tilde{h}$ , and hence large  $\alpha$ , already

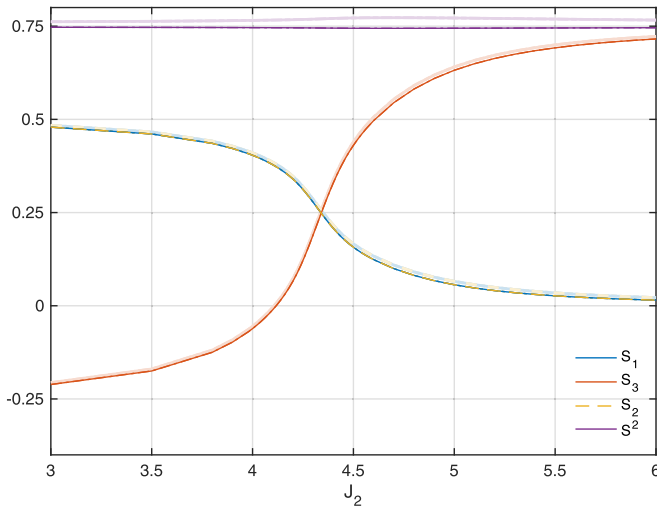


FIG. 10. Local DMRG expectation values as in Eqs. (C1) with a focus on the presence of a nematic phase for the full Hamiltonian (1) for  $L = 64$  and  $J = [1, J_2, 4]$ , as also analyzed in Fig. 2, having  $S^2 \equiv S_1 + S_2 + S_3$ . Light colors use the full local spin operators  $\mathbf{S}_m$ , whereas strong colors use the projected spin operators  $\mathbf{S}_m$ , as reflected in Eqs. (C1). The ground state is the same in either case, hence it also includes the local  $S = 3/2$  multiplet.

also applies in the original Hamiltonian (3) in the main text, and hence is not constrained to the mean-field analysis here.

### APPENDIX C: ABSENCE OF $\mathbb{Z}_2$ SYMMETRY BREAKING IN DMRG

In the strong-coupling limit, we have [cf. Eqs. (A6)]

$$S_m \equiv \langle \mathbf{S}_m \cdot \mathcal{S} \rangle_i = \frac{2s^2}{3} \left( \frac{1}{2} + \langle \mathcal{T}_i^z \rangle \pm \sqrt{3} \langle \mathcal{T}_i^x \rangle \right) \quad (m = 1, 2),$$

$$S_3 \equiv \langle \mathbf{S}_3 \cdot \mathcal{S} \rangle_i = \frac{2s^2}{3} \left( \frac{1}{2} - 2 \langle \mathcal{T}_i^z \rangle \right), \quad (\text{C1})$$

where  $s^2$  is the spectral weight in the spin sector. Therefore,  $S_1$  can be negative only in the nematic phase, whereas  $S_3 < 0$  is permitted more generically, namely when  $\langle \mathcal{T}_i^z \rangle > 1/4$ .

We evaluated the expectation values in Eqs. (C1) using DMRG, with the results summarized in Fig. 10. Given that  $S_1$  and  $S_2$  stay positive, there is clearly no support for a nematic phase. In addition, the data for  $S_1$  and  $S_2$  lies exactly on top of each other, which thus also demonstrates that the rung exchange symmetry is preserved. The local expectation value  $S_3$  can become negative, but that simply reflects orbital polarization. As already seen with Fig. 2 in the main text, dimerization is only visible for expectation values that stretch

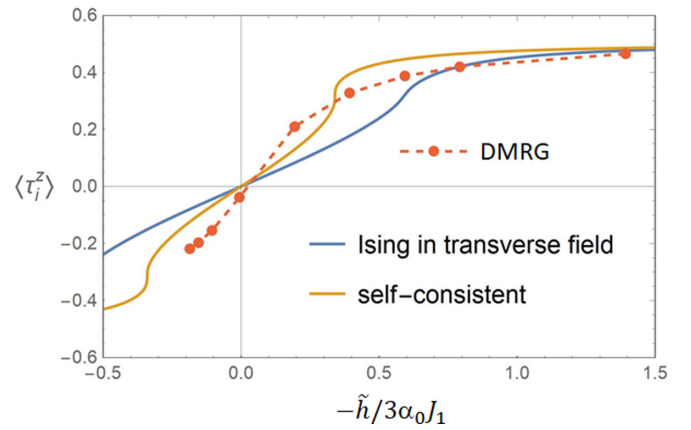


FIG. 11. Comparison of the orbital expectation value  $\langle \mathcal{T}_i^z \rangle$  vs  $\tilde{h}$  between DMRG and SMF: DMRG data as in Fig. 10, the exact mean-field solution of Eq. (B3a) in the absence of the  $\langle \mathcal{T}_i^z \rangle$  term (i.e., the Ising model in a transverse field [44]), and the self-consistent mean-field theory for Eq. (B3a).

along the system. For expectation values within individual rungs, these data is the same for even and odd rungs, i.e., they do not display dimerization in itself. This also holds in the present case for the data in Fig. 10.

Adding up the data,  $S_1 + S_2 + S_3 = S^2$ , this yields the expectation value of the total spin operator (also labeled  $S^2$  in Fig. 10), which is approximately constant, having  $S^2 \approx 0.75$ . This demonstrates that the present parameter setting with  $J_3 = 4$  is deep within the strong rung-coupling regime, in that the local density matrix is overwhelmingly dominated by the  $S = 1/2$  multiplets. The  $S^2$  data displayed in light color reaches slightly above 0.75, which shows that they also include a weak  $S = 3/2$  component. The  $S^2$  data is displayed in strong color are slightly deficient of 0.75, because it refers to the projected spin operators.

Overall, our DMRG data here again finds no evidence for the  $\mathbb{Z}_2$ -symmetry-broken phase with  $\langle \mathcal{T}_i^x \rangle \neq 0$  near  $\tilde{h} = 0$ , as suggested by a semi-mean-field analysis on a uniform system. Instead, bond dimerization is found. To evaluate what has been missed in the SMF analysis assuming translational invariance, we compare the obtained  $\langle \mathcal{T}_i^z \rangle$  with the DMRG result, as shown in Fig. 11. The vertical slopes that indicate the phase boundaries of the intermediate  $\mathbb{Z}_2$ -broken phase in the self-consistent SMF analysis are entirely absent in the DMRG data, which evolves smoothly throughout. The considerably stronger  $\langle \mathcal{T}_i^z \rangle$  values in the DMRG data near  $\tilde{h} = 0$  suggest that the semi-mean-field theory needs to allow for bond dimerization, as discussed in the main text.

- [1] J. Wilkens and H. Müller-Buschbaum, Zur kenntnis von  $\text{Ba}_4\text{Ir}_3\text{O}_{10}$ , *Z. Anorg. Allg. Chem.* **592**, 79 (1991).
- [2] K. E. Stitzer, M. D. Smith, and H.-C. Loye, Crystal growth, structure determination and magnetic properties of  $\text{Ba}_4\text{Ir}_3\text{O}_{10}$  and  $\text{Ba}_4(\text{Co}_{0.4}\text{Ir}_{0.6})\text{Ir}_2\text{O}_{10}$ , *J. Alloys Compd.* **338**, 104 (2002), Special Issue to Honor Professor H. Fritz Franzen.

- [3] G. Cao *et al.*, Quantum liquid from strange frustration in the trimer magnet  $\text{Ba}_4\text{Ir}_3\text{O}_{10}$ , *npj Quantum Mater.* **5**, 26 (2020).
- [4] L. T. Nguyen and R. J. Cava, Hexagonal perovskites as quantum materials, *Chem. Rev.* (2020), doi: [10.1021/acs.chemrev.0c00622](https://doi.org/10.1021/acs.chemrev.0c00622).
- [5] M. Kohno, O. A. Starykh, and L. Balents, Spinons and triplons in spatially anisotropic frustrated antiferromagnets, *Nat. Phys.* **3**, 790 (2007).

- [6] W. Yin, Frustration-driven marginal phase transition at finite temperature in a one-dimensional ladder Ising model, [arXiv:2006.08921](#).
- [7] W. Yin, Finding and classifying an infinite number of cases of the marginal phase transition in one-dimensional Ising models, [arXiv:2006.15087](#).
- [8] C. K. Majumdar and D. K. Ghosh, On next-nearest-neighbor interaction in linear chain. i, *J. Math. Phys.* **10**, 1388 (1969).
- [9] S. R. White and I. Affleck, Dimerization and incommensurate spiral spin correlations in the zigzag spin chain: Analogies to the Kondo lattice, *Phys. Rev. B* **54**, 9862 (1996).
- [10] J.-B. Fouet, A. Läuchli, S. Pilgram, R. M. Noack, and F. Mila, Frustrated three-leg spin tubes: From spin 1/2 with chirality to spin 3/2, *Phys. Rev. B* **73**, 014409 (2006).
- [11] S. Nishimoto and M. Arikawa, Basic properties of three-leg Heisenberg tube, *J. Phys.: Conf. Ser.* **145**, 012041 (2009).
- [12] N. B. Ivanov, J. Schnack, R. Schnalle, J. Richter, P. Kogerler, G. N. Newton, L. Cronin, Y. Oshima, and H. Nojiri, *Phys. Rev. Lett.* **105**, 037206 (2010).
- [13] S. R. White, Density Matrix Formulation for Quantum Renormalization Groups, *Phys. Rev. Lett.* **69**, 2863 (1992).
- [14] U. Schollwöck, The density-matrix renormalization group in the age of matrix product states, *Ann. Phys.* **326**, 96 (2011).
- [15] I. A. Zaliznyak, C. Broholm, M. Kibune, M. Nohara, and H. Takagi, Anisotropic Spin Freezing in the  $S = 1/2$  Zigzag Chain Compound SrCuO<sub>2</sub>, *Phys. Rev. Lett.* **83**, 5370 (1999).
- [16] S. R. White, Numerical canonical transformation approach to quantum many-body problems, *J. Chem. Phys.* **117**, 7472 (2002).
- [17] W.-G. Yin and W. Ku, Tuning the in-plane electron behavior in high- $T_c$  cuprate superconductors via apical atoms: A first-principles Wannier-states analysis, *Phys. Rev. B* **79**, 214512 (2009).
- [18] W.-G. Yin and W. Ku, A novel first-principles approach to effective hamiltonians for high  $T_c$  superconducting cuprates, *J. Phys.: Conf. Ser.* **108**, 012032 (2008).
- [19] W.-G. Yin, D. Volja, and W. Ku, Orbital Ordering in lamno<sub>3</sub>: Electron-Electron Versus Electron-Lattice Interactions, *Phys. Rev. Lett.* **96**, 116405 (2006).
- [20] W.-G. Yin *et al.*, Ferromagnetic Exchange Anisotropy from Antiferromagnetic Superexchange in the Mixed  $3d - 5d$  Transition-Metal Compound Sr<sub>3</sub>CuIrO<sub>6</sub>, *Phys. Rev. Lett.* **111**, 057202 (2013).
- [21] A. E. Feiguin, A. M. Tsvelik, W. Yin, and E. S. Bozin, Quantum Liquid with Strong Orbital Fluctuations: The Case of a Pyroxene Family, *Phys. Rev. Lett.* **123**, 237204 (2019).
- [22] J. Hubbard and B. H. Flowers, Electron correlations in narrow energy bands - iv. the atomic representation, *Proc. R. Soc. London, Ser. A* **285**, 542 (1965).
- [23] E. Dagotto, T. Hotta, and A. Moreo, Colossal magnetoresistant materials: The key role of phase separation, *Phys. Rep.* **344**, 1 (2001).
- [24] A. Moreo, S. Yunoki, and E. Dagotto, Phase separation scenario for manganese oxides and related materials, *Science* **283**, 2034 (1999).
- [25] M. Imada, A. Fujimori, and Y. Tokura, Metal-insulator transitions, *Rev. Mod. Phys.* **70**, 1039 (1998).
- [26] W.-G. Yin, H.-Q. Lin, and C.-D. Gong, Single Hole Motion in LaMnO<sub>3</sub>, *Phys. Rev. Lett.* **87**, 047204 (2001).
- [27] C. D. Batista, J. E. Gubernatis, and W.-G. Yin, Electronic mechanism for the coexistence of ferroelectricity and ferromagnetism, *Phys. Rev. B* **75**, 014423 (2007).
- [28] W.-G. Yin, C.-C. Lee, and W. Ku, Unified Picture for Magnetic Correlations in Iron-Based Superconductors, *Phys. Rev. Lett.* **105**, 107004 (2010).
- [29] L. Hulthén, Über das Austauschproblem eines Kristalles, *Ark. Mat. Astron. Fys. B.* **26A**, 1 (1938).
- [30] H. Bethe, Zur theorie der metalle, *Z. Phys.* **71**, 205 (1931).
- [31] A. Weichselbaum, S. Capponi, P. Lecheminant, A. M. Tsvelik, and A. M. Läuchli, Unified phase diagram of antiferromagnetic SU(N) spin ladders, *Phys. Rev. B* **98**, 085104 (2018).
- [32] K. Kawano and M. Takahashi, Three-leg antiferromagnetic Heisenberg ladder with frustrated boundary condition; ground state properties, *J. Phys. Soc. Jpn.* **66**, 4001 (1997).
- [33] S. R. White and A. E. Feiguin, Real-Time Evolution Using the Density Matrix Renormalization Group, *Phys. Rev. Lett.* **93**, 076401 (2004).
- [34] A. J. Daley, C. Kollath, U. Schollwöck, and G. Vidal, Time dependent density matrix renormalization group using adaptive effective Hilbert spaces, *J. Stat. Mech.: Theor. Exp.* (2004) P04005.
- [35] T. Barthel, U. Schollwöck, and S. R. White, Spectral functions in one-dimensional quantum systems at finite temperature using the density matrix renormalization group, *Phys. Rev. B* **79**, 245101 (2009).
- [36] S. Lukyanov, Low energy effective Hamiltonian for the XXZ spin chain, *Nucl. Phys. B* **522**, 533 (1998).
- [37] S. Lukyanov and A. Zamolodchikov, Exact expectation values of local fields in the quantum sine-gordon model, *Nucl. Phys. B* **493**, 571 (1997).
- [38] I. Affleck and F. D. M. Haldane, Critical theory of quantum spin chains, *Phys. Rev. B* **36**, 5291 (1987).
- [39] A. M. Tsvelik, *Quantum Field Theory in Condensed Matter Physics* (Cambridge University Press, Cambridge, 2003) Chap. 16.
- [40] A. M. Tsvelik and I. A. Zaliznyak, Heisenberg necklace model in magnetic field, *Phys. Rev. B* **94**, 075152 (2016).
- [41] F. Haldane, Continuum dynamics of the 1-d Heisenberg antiferromagnet: Identification with the O(3) nonlinear sigma model, *Phys. Lett. A* **93**, 464 (1983).
- [42] A. Polyakov and P. Wiegmann, Theory of nonabelian goldstone bosons in two dimensions, *Phys. Lett. B* **131**, 121 (1983).
- [43] A. Zamolodchikov and A. Zamolodchikov, Massless factorized scattering and sigma models with topological terms, *Nucl. Phys. B* **379**, 602 (1992).
- [44] P. Pfeuty, The one-dimensional ising model with a transverse field, *Ann. Phys.* **57**, 79 (1970).
- [45] E. Lieb, T. Schultz, and D. Mattis, Two soluble models of an antiferromagnetic chain, *Ann. Phys.* **16**, 407 (1961).